horticulturae

MDPI

Article

RGB-Based Estimation of Chlorophyll-Fluorescence-Derived Photochemical Status Across Garden Plant Species Under Progressive Drought

Seong Ju Lee [1], Tae Seon Eom [1], Tae Wan Kim [1,2,*] and Sung Yung Yoo [2,*]

[1] Department of Plant Resources and Landscape Architecture, Hankyong National University, Anseong-si 17579, Republic of Korea; leesj9691@naver.com (S.J.L.); ymh5240@hknu.ac.kr (T.S.E.)
[2] Institute of Ecological Phytochemistry, Hankyong National University, Anseong-si 17579, Republic of Korea
* Correspondence: taewkim@hknu.ac.kr (T.W.K.); lsn136@hknu.ac.kr (S.Y.Y.)

Highlights

What are the main findings?

- A Photochemical Status Index (PSI) summarized the shared variation among five highly correlated JIP-test energy-flux variables.
- Five RGB-derived predictors—g, GLI, ExG, ExGR, and CIVE—were selected in all ten outer folds of nested leave-one-species-out validation.
- The final PLSR model captured a moderate portion of out-of-species PSI variation (R^2 = 0.469, RMSE = 1.585, and MAE = 1.183).

What are the implications of the main findings?

- Predictive performance varied substantially among species, and predictions were compressed toward the center of the PSI range.
- The results provide fluorescence-referenced proof-of-concept evidence; external validation is required before practical deployment.

Abstract

Chlorophyll fluorescence provides sensitive information on plant photochemical responses, but its measurement requirements can limit high-throughput application. This study investigated whether RGB imagery could approximate chlorophyll-fluorescence-derived photochemical status across garden plant species during progressive soil drying. A Photochemical Status Index (PSI) was constructed by principal component analysis from five highly correlated JIP-test energy-flux variables (RC/CS, ABS/CS, TRo/CS, ET2o/CS, and RE1o/CS). The dataset comprised 50 aggregated species-by-soil-moisture-stage observations representing ten species and five sequential soil-moisture stages. Eleven RGB-derived variables were evaluated, and a partial least-squares regression model was assessed using nested leave-one-species-out validation, with all data-dependent procedures repeated within each outer training fold. PC1 explained 96.5% of the shared variation among the fluorescence-derived fluxes. The predictors g, GLI, ExG, ExGR, and CIVE were retained in all ten outer folds. The final model yielded a pooled out-of-fold R^2 of 0.469, an RMSE of 1.585, and an MAE of 1.183. However, species-specific R^2 ranged from −0.179 to 0.959, and a calibration slope of 0.509 indicated prediction-range compression. These findings provide proof-of-concept evidence of moderate RGB-based approximation of fluorescence-derived photochemical status, but inconsistent species transferability and the common soil-moisture/time gradient require external validation before practical deployment.

Academic Editor: Lucia Guidi

Received: 21 July 2026
Revised: 14 August 2026
Accepted: 25 August 2026
Published: 27 August 2026

Keywords: garden plants; progressive drought; chlorophyll fluorescence; JIP-test; RGB imaging; Photochemical Status Index (PSI); partial least-squares regression; nested leave-one-species-out validation

1. Introduction

Accurate assessment of plant responses to drought has become increasingly important as drought events intensify under ongoing climate change, threatening the sustainable management of ornamental landscapes worldwide [1–3]. Declining soil water availability can induce interacting responses involving stomatal regulation, carbon assimilation, photochemistry, electron transport, osmotic adjustment, and biochemical metabolism, with their relative contributions varying among species and with drought severity [4–8]. Although many of these responses can precede visible symptoms such as wilting, chlorosis, and growth inhibition, prolonged or severe water deficits may eventually cause persistent physiological impairment and deterioration of ornamental quality [9–11]. Therefore, detecting drought-induced changes before visible damage occurs is important for timely irrigation management. This need is particularly relevant in ornamental landscapes, where species with contrasting drought-response strategies and water requirements are cultivated together. Such biological diversity complicates irrigation management and highlights the need for approaches capable of assessing comparable drought-responsive processes across multiple species.

Among the processes affected by drought, photosynthetic function is particularly sensitive to declining water availability [12–14]. Drought-induced limitations to photosynthesis may involve stomatal restriction of CO_2 diffusion, biochemical constraints on carbon fixation, and alterations in photochemical energy conversion and electron transport [5,15–18]. These processes may occur concurrently rather than in a fixed temporal sequence, and their relative importance depends on species, drought intensity, and stress duration. Under sufficiently severe or prolonged drought, imbalances between absorbed light energy and its utilization may reduce photochemical efficiency and impair photosystem II (PSII) and the photosynthetic electron transport chain [5,15,16]. Chlorophyll fluorescence analysis is therefore widely used to evaluate drought-induced changes in the photosynthetic apparatus [19,20]. Among fluorescence techniques, OJIP transient analysis provides information on several components of PSII-related energy flux, including light absorption, excitation energy trapping, electron transport, and reduction in terminal electron acceptors [21–23]. Previous studies have used chlorophyll fluorescence parameters, including Fv/Fm and OJIP-derived performance indices, to characterize drought-induced changes in photosynthetic performance across diverse plant species [24–30]. Nevertheless, chlorophyll fluorescence measurements require specialized instrumentation and generate numerous interrelated parameters whose joint interpretation can be complex, limiting their use for rapid and large-scale monitoring under practical field and landscape conditions [31–33].

To address the practical limitations of instrument-based physiological measurements, RGB imaging has emerged as an attractive approach for plant stress monitoring because it is inexpensive, non-destructive, and readily applicable to large-scale phenotyping and field conditions [34–36]. Unlike chlorophyll fluorescence, RGB imaging records visible optical characteristics associated with changes in leaf color, pigment composition, and canopy appearance under environmental stress [37–39]. Previous studies have related RGB-derived vegetation indices to leaf chlorophyll content [40], used RGB imagery to estimate multispectral vegetation indices in wheat [41], and applied RGB-based indices to monitor crop growth [42]. RGB indices have also been associated with fluorescence-derived Fv/Fm under

drought and salinity conditions [36]. These findings demonstrate that visible image features can covary with specific plant traits and stress responses, although they do not establish that RGB imagery directly measures whole-plant physiological status. Nevertheless, the affordability and scalability of RGB imaging have promoted its application in precision agriculture, high-throughput phenotyping, and automated crop monitoring [43–49]. Whether RGB-derived indices can estimate a continuous, fluorescence-derived representation of drought-associated photochemical variation across species remains insufficiently evaluated.

Our previous study, based on the same greenhouse experiment, combined RGB indices and chlorophyll fluorescence variables to identify discrete groups of species exhibiting different drought-response patterns and evaluated whether these categorical groups could be classified using an SVM model [50]. The present study addresses a distinct question. Rather than classifying species into predefined response groups, we integrated five OJIP energy-flux parameters into a continuous latent axis representing their shared drought-associated photochemical variation and examined whether this continuous target could be estimated from RGB-derived indices. We further evaluated transferability to previously unseen species using leave-one-species-out cross-validation, with predictor selection performed independently within each training fold. We therefore hypothesized that drought-associated changes in visible plant characteristics captured by conventional RGB imagery covary with the shared variation among OJIP-derived energy-flux parameters. Specifically, this study aimed to (i) construct an integrated photochemical index from representative OJIP parameters, (ii) quantify its relationships with RGB-derived vegetation indices, and (iii) develop and evaluate an RGB-based proxy for estimating drought-associated photochemical status across multiple garden plant species.

2. Materials and Methods

2.1. Overall Research Framework

The overall workflow for developing and evaluating the RGB-based photochemical proxy is illustrated in Figure 1. First, the greenhouse drought experiment provided two complementary datasets collected during the same experimental period: chlorophyll-fluorescence OJIP measurements and RGB images. Five JIP-test energy-flux variables derived from the OJIP measurements were integrated using principal component analysis (PCA) to construct the Photochemical Status Index (PSI). The RGB images were processed using the developed image-analysis workflow to extract RGB-derived variables, including established vegetation indices and normalized RGB channel ratios.

Exploratory relationships between PSI and the RGB-derived variables were initially examined using Pearson correlation and simple linear regression. The RGB-based photochemical proxy was subsequently developed and evaluated using partial least-squares regression (PLSR) within a nested leave-one-species-out (LOSO) framework. In each outer fold, one species was withheld as an independent test set, while Pearson screening, predictor standardization, selection of the number of PLS components, variable importance in projection (VIP) analysis, and final model fitting were conducted exclusively using data from the remaining species. The fitted model was then applied to the completely held-out species. Predictions from all outer folds were pooled to evaluate out-of-species predictive performance, and fold-specific results were examined descriptively to assess variation among held-out species. After completion of nested LOSO validation, an implementation equation was refitted using the complete dataset and the predictors consistently selected across the outer folds. This complete-data fit was used only to derive implementation coefficients and was kept separate from the nested LOSO estimate of predictive performance.

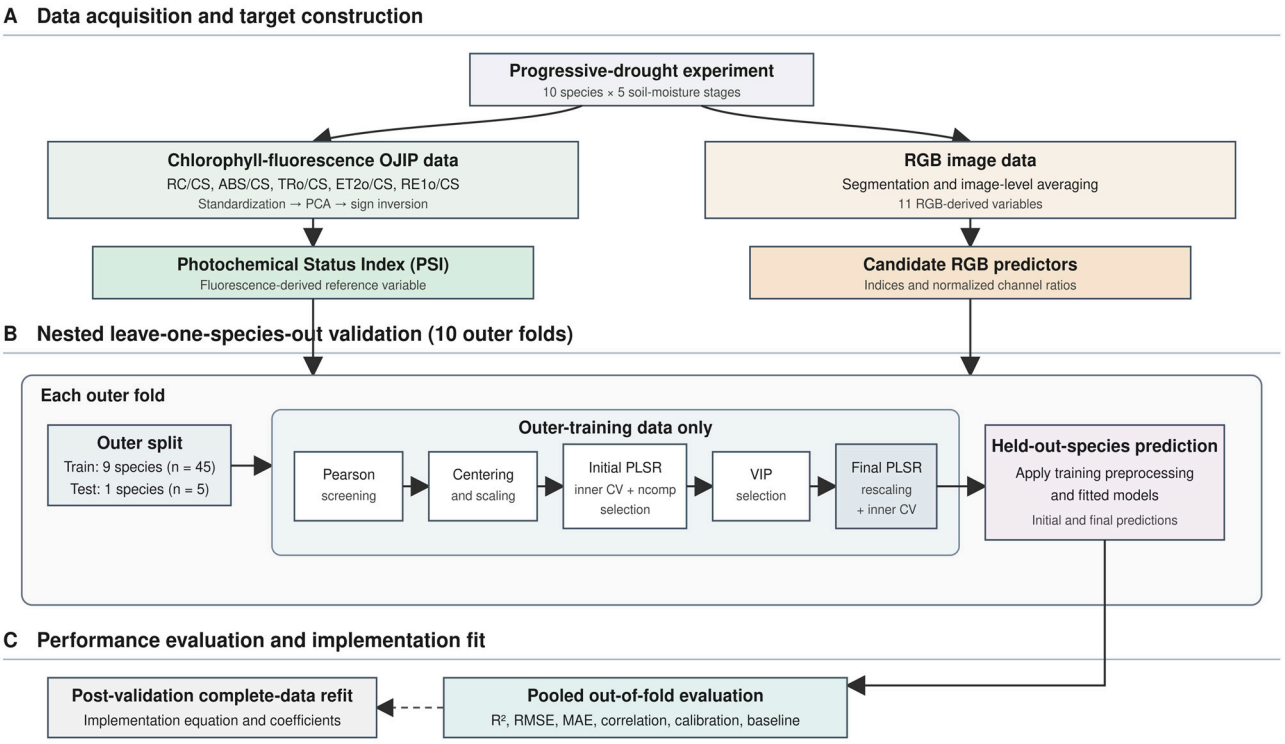

Figure 1. Overall workflow for the development and evaluation of the RGB-based photochemical proxy. Five JIP-test energy-flux variables were integrated by PCA to construct the Photochemical Status Index (PSI), while RGB images were processed to obtain 11 RGB-derived candidate variables. Model development and validation were performed using nested leave-one-species-out cross-validation. Pearson screening, predictor standardization, component selection, VIP calculation, and model fitting were conducted independently within each outer training fold before prediction of the completely held-out species. Out-of-fold predictions were pooled to estimate predictive performance. After validation, a separate complete-data fit was performed only to obtain the implementation equation and coefficients.

2.2. Experimental Dataset

The dataset used in this study was obtained from a greenhouse drought experiment conducted from 15 July to 24 August 2023 at the Hankyong National University Affiliated Farm, Anseong, Republic of Korea. Ten garden plant species were examined, with three individually potted plants per species serving as biological replicates, resulting in 30 experimental units (Table 1). Each pot measured 143 × 143 × 160 mm (L × W × H) and was filled with silty loam. During a 15-day acclimatization period, the plants were irrigated daily for 30 min beginning at 08:00 using individual drip stakes. Control measurements were conducted at 15 days after transplanting (DAT), and normal irrigation was continued until the scheduled irrigation was withheld at 20 DAT. Greenhouse temperature was recorded hourly using a testo 174 H data logger (Testo Saveris GmbH, Baden-Württemberg, Germany). During the experiment, daily mean greenhouse temperature ranged from 22.3 to 39.9 °C, with an overall mean of 31.6 °C. Volumetric water content (VWC) was measured hourly in four randomly selected pots using WaterScout SM 100 sensors connected to WatchDog 1000 Series data loggers (Spectrum Technologies, Inc., Aurora, IL, USA), and the values from the four pots were averaged. Additional details of the original experiment and environmental conditions are provided in Ref. [50].

Table 1. List of the ten garden plant species used in the experiment.

Scientific Name	English Name	Scientific Name	English Name
Polygonatum odoratum	Lesser solomon's seal	*Phedimus takesimensis*	Ulleungdo stonecrop
Pachysandra terminalis	Carpet box	*Iris sanguinea*	Blood iris
Hosta plantaginea	Fragrant plantain lily	*Lilium lancifolium*	Tiger lily
Aster spathulifolius	Seashore spatulate aster	*Carex maculata*	Maculate sedge
Mukdenia rossii	Maple-leaf mukdenia	*Allium dumebuchum*	Aging chive

The VWC values of 31.0, 21.5, 7.4, 6.1, and 4.6% were not independently imposed treatments but sequential sampling stages obtained from the same set of experimental pots during progressive drying. Chlorophyll-fluorescence measurements were conducted between 14:00 and 15:00 at 15, 20, 25, 30, and 35 DAT, corresponding to 30 July and 4, 9, 14, and 19 August 2023, respectively. The scheduled morning irrigation was first omitted at 20 DAT, before measurement of the 21.5% VWC stage. Because VWC declined progressively after irrigation withdrawal, it inherently covaried with elapsed time and associated temporal changes in plant and canopy characteristics.

At each sampling stage, chlorophyll fluorescence was measured on the third and fourth fully expanded leaves from the apex in each of the three pots, yielding six measurements per species. These measurements were averaged to obtain one fluorescence observation for each species-by-stage combination. On each sampling date, three fixed time-lapse cameras simultaneously recorded their respective plant groups five times between 11:00 and 15:00. Two camera views each contained four species, corresponding to 12 pots per frame, whereas the third contained two species, corresponding to 6 pots per frame; each species was represented by three pots. Species-specific rectangular regions of interest containing the three pots of each species were extracted from these group-level frames. The RGB outputs from the three pots and 12 image orientations were aggregated to obtain one hourly species-level estimate, and the five hourly estimates were then averaged to obtain one sampling-date species-level RGB value. The three pots per species were biological replicates that contributed to each aggregated RGB and fluorescence value, but they were not retained as separate analytical observations. The RGB and fluorescence data were therefore paired at the species-by-sampling-stage level rather than at the individual-pot or individual-leaf level. The final dataset comprised 50 paired observations (10 species $\times$ 5 sequential sampling stages).

2.3. Construction of the Photochemical Status Index (PSI)

Five OJIP-derived energy-flux parameters were used to construct a continuous latent variable representing their shared drought-associated photochemical variation: RC/CS, the density of Q_a-reducing active PSII reaction centers per excited leaf cross-section; ABS/CS, the absorption flux per excited leaf cross-section; TRo/CS, the trapped excitation-energy flux at t = 0 per excited leaf cross-section; ET2o/CS, the electron-transport flux at t = 0 per excited leaf cross-section; and RE1o/CS, the electron-transport flux reaching photosystem I end acceptors at t = 0 per excited leaf cross-section. Here, CS denotes the excited leaf cross-section. Their operational calculations are summarized in Table 2. Because these phenomenological fluxes are derived from the same OJIP transient and share ABS/CS and related quantum-yield terms in their calculations, they are mathematically and structurally interdependent. Their high covariance was therefore interpreted as shared variation within a common photochemical energy-flux system rather than as evidence that five physiologically independent processes had been measured.

Table 2. Definitions and formulas of the OJIP-derived JIP-test parameters used to construct the Photochemical Status Index.

Parameter	Descriptions
$RC/CS_x=\varphi_{P_O}(V_J/M_O)(ABS/CS_x)$	Density of RCs (Q_A-reducing PSII reaction centers)
ABS/CS_x	Absorption flux per CS 'x' can be 'Chl', 0 or 'M'
$TR_O/CS_x = \varphi_{P_O}(ABS/CS_x)$	Trapped energy flux per CS (at t = 0)
$ET2_O/CS_x = \varphi_{E_O}(ABS/CS_x)$	Electron transport flux per CS (at t = 0)
$RE1_O/CS_x = \varphi_{RE1_O}(ABS/CS_x)$	Electron transport flux until PSI acceptors per CS (at t = 0)

CS denotes the excited leaf cross-section. The /CS parameters are relative phenomenological quantities derived from fluorescence signals and are therefore expressed on a relative scale rather than in absolute physical energy units.

The five parameters were identified in our previous study [51] using Pearson correlation analysis, principal component analysis, and relative-importance analysis applied to chlorophyll-fluorescence measurements obtained from the same underlying greenhouse experiment used in the present study. Therefore, their selection was not based on an independent dataset. In the present analysis, these variables were used as a predefined subset of OJIP energy-flux parameters to construct a continuous latent photochemical target. The resulting index was regarded as an internally derived summary of the selected fluorescence variables rather than as an independently validated measure of whole-plant physiological status.

Principal component analysis was performed in R (version 4.1.2) using prcomp(x, center = TRUE, scale. = TRUE). Each parameter was therefore centered by its sample mean and scaled by its sample standard deviation once within the prcomp() procedure before decomposition. Because the algebraic sign of a principal component is arbitrary, the PC1 scores were multiplied by -1 so that higher values corresponded to relatively greater maintenance of the selected photochemical energy fluxes and lower values corresponded to their shared decline. The sign-reversed PC1 score was designated the Photochemical Status Index (PSI). PSI is a centered, dimensionless, and dataset-dependent relative score rather than an absolute physiological or stress scale. Accordingly, positive and negative PSI values indicate positions above or below the dataset mean along the latent photochemical axis and do not represent absolute thresholds of plant health or injury.

Because PCA was conducted across all ten species, PSI distributions were examined across species and sequential sampling stages. A linear model including sampling stage and species as fixed effects was fitted to distinguish variation associated with the progressive-drying sequence from baseline interspecific variation.

For observation i, PSI was calculated as:

$$\text{Photochemical Status Index (PSI)} = -\sum_{j=1}^{5} l_j \left(\frac{x_{ij} - \overline{x}_j}{S_j} \right) \quad (1)$$

where x_{ij} is the observed value of parameter j, $\overline{x_j}$ and S_j are its sample mean and sample standard deviation, respectively, and l_j is its PC1 loading. The negative sign reflects the reversal of the arbitrary PC1 orientation described above.

2.4. RGB Image Processing and RGB-Derived Variable Extraction

RGB images were acquired using three fixed time-lapse cameras of the same model (TLC200, Brinno Inc., Taipei City, Taiwan; firmware version 1.02.5) mounted on fixed pipes approximately 2 m above their respective plant groups, as described in our previous study [50]. Two camera fields of view each contained four species, corresponding to 12 pots per frame, whereas the third contained two species, corresponding to 6 pots per frame. Each

species was represented by three pots. The camera positions, imaging heights, and fields of view were maintained throughout the experiment. The cameras were operated in Daylight scene mode, with image quality set to Best, exposure compensation maintained at its central setting, low-light recording enabled, and the band filter disabled. Images were recorded hourly from 11:00 to 15:00 at an output resolution of 1280 × 720 pixels. The TLC200 cameras did not provide user-accessible controls for independently specifying white balance, ISO, or shutter speed; these parameters were handled internally by each camera, and their frame-specific values were not recorded. The time-lapse recordings were converted to JPEG images using Brinno Video Player. The extracted images had a 24-bit RGB color depth (8 bits per channel), corresponding to R, G, and B digital numbers ranging from 0 to 255. No color or gray reference was included during image acquisition, and no post-acquisition radiometric calibration or illumination normalization was applied. Accordingly, the extracted RGB values represent camera-processed digital numbers rather than calibrated reflectance values. Consequently, temporal variation in greenhouse illumination and the cameras' internal exposure and white-balance processing could have affected the RGB digital numbers and the indices derived from them. Ratio-based variables may reduce sensitivity to uniform changes in overall brightness, but they do not eliminate the effects of changes in illumination spectrum or channel-specific camera processing; indices calculated directly from 8-bit R, G, and B values may be particularly sensitive to these effects. Because the species were distributed among three fixed camera fields of view, apparent differences among species could also partly reflect camera-specific responses or spatial differences in illumination, in addition to genuine differences in plant color, morphology, and canopy structure. Averaging the five hourly acquisitions reduced the influence of individual frames but did not constitute radiometric calibration.

Image processing was performed separately for each species using R. Each group-level frame was divided into species-specific rectangular regions of interest, with each region containing the three pots of the corresponding species. The regions of interest were defined according to the fixed location and spatial extent of each species within the camera field of view; no other species-specific segmentation rules were applied. Only images acquired on the five chlorophyll-fluorescence sampling dates were used in the paired RGB–PSI analyses. This corresponded to 75 original group-level frames (3 cameras × 5 acquisition times × 5 sampling dates) and 250 species-specific cropped source images (10 species × 5 acquisition times × 5 sampling dates). Each cropped source image was processed at 12 in-plane orientations from 0° to 330° at 30° intervals. The complete segmentation and RGB-variable extraction procedure was repeated independently after each rotation. The overall image-processing workflow, from species-specific cropping through in-plane rotation and RGB-derived index calculation, is illustrated in Figure 2. The rotation procedure was not expected to alter an RGB variable calculated from an identical fixed set of plant pixels. However, because the complete segmentation procedure was repeated after each rotation, the observed orientation-dependent variation could reflect the combined effects of raster resampling, possible interpolation at object boundaries, changes in pixel connectivity, and differences in the resulting segmentation masks. These effects were not separated individually in the present analysis.

For segmentation, normalized RGB ratios were used as input to k-means clustering with k = 9. To reduce computational demand, a maximum area of 5000 pixels was sampled from each processed image. The clustering procedure was performed using a fixed random seed (set.seed(1)) and 10 random initializations (nstart = 10). Clusters representing plant material were identified using the color-separation criterion ($|r - g| + |g - b| > 0.15$). Pixels with brightness values below the image-specific 10th percentile were excluded to reduce the influence of shadows. The resulting binary mask was refined by morphological

closing using a disc-shaped structuring element with a diameter of 15 pixels, and connected components smaller than 2000 pixels were removed. All resulting segmentation masks were visually inspected across the complete progressive-drying sequence, including the initial well-watered condition and later drought-affected stages, to identify evident processing failures and assess whether the detected regions corresponded to visible plant material. This quality control was qualitative; quantitative segmentation accuracy was not calculated because manually annotated ground-truth masks were unavailable.

Mean 8-bit R, G, and B digital numbers were extracted from each detected plant region and used to calculate the 11 RGB variables defined in Table 3: the normalized channel ratios r, g, and b, and the eight color indices BGI, GLI, NGRDI, ExG, ExR, ExGR, CIVE, and VARI. All variables were therefore derived from the same camera-processed R, G, and B digital numbers. The normalized channel ratios were calculated by dividing each channel by (R + G + B). BGI, GLI, NGRDI, and VARI were calculated as ratio-based combinations of the RGB channels, whereas ExG, ExR, ExGR, and CIVE were calculated directly from the 8-bit R, G, and B digital-number scale.

Table 3. RGB-derived vegetation indices and color features used in this study.

No.	Index	Descriptions	Formula
1	BGI [52]	Blue Green Pigment Index	B/G
2	GLI [53]	Green Leaf Index	$(2{\cdot}G - R - B)/(2{\cdot}G + R + B)$
3	NGRDI [54]	Normalized Green Red Difference Index	$(G - R)/(G + R)$
4	ExG [55]	Excess Green Index	$2{\cdot}G - R - B$
5	ExR [56]	Excess Red Index	$1.4{\cdot}R - G$
6	ExGR [56]	Excess Green minus Excess Red Index	$3{\cdot}G - 2.4{\cdot}R - B$
7	CIVE [57]	Color Index of Vegetation Extraction	$0.441{\cdot}R - 0.811{\cdot}G + 0.385{\cdot}B + 18.787$
8	VARI [58]	Visible Atmospherically Resistant Index	$(G - R)/(G + R - B)$
9	r	Normalized Red	$R/(R + G + B)$
10	g	Normalized Green	$G/(R + G + B)$
11	b	Normalized Blue	$B/(R + G + B)$

For each species-specific cropped source image, outputs from all detected plant regions across the 12 orientations were pooled separately for each of the 11 RGB variables. Extreme processing outputs were excluded using the 1.5 × interquartile-range criterion, and the remaining values were averaged to obtain one hourly species-level estimate for each variable. The detected-region identifiers were used only to distinguish connected components within each processed orientation and were not treated as persistent pot identities across rotations. The detected plant regions associated with the three biological replicate pots contributed to the aggregated estimate but were not retained as three independent pot-level observations. Neither the detected-region outputs nor the orientation-specific outputs were treated as independent analytical observations. The five hourly species-level estimates obtained from 11:00 to 15:00 were subsequently averaged to generate one sampling-date species-level RGB value. On each physiological sampling date, this RGB value was paired with the corresponding species-level mean chlorophyll-fluorescence measurement, which had also been averaged across the three pots. The resulting analytical dataset comprised 50 paired observations (10 species × 5 sequential sampling stages).

As a sensitivity analysis, orientation-dependent variation was evaluated using the 1369 source images from all ten species for which valid outputs were available for all 12 orientations and all 11 RGB variables. Within each source image and orientation, outputs from all detected plant regions were first averaged. For each RGB variable, the standard deviation and range across the 12 orientation-level means and the absolute difference between the unrotated (0°) output and the corresponding 12-orientation mean were then calculated.

These quantities were summarized across source images using the median and interquartile range (Table A1). This analysis evaluated the sensitivity of the segmentation-derived RGB-index outputs to in-plane orientation; it was not intended to assess segmentation accuracy or predictive performance.

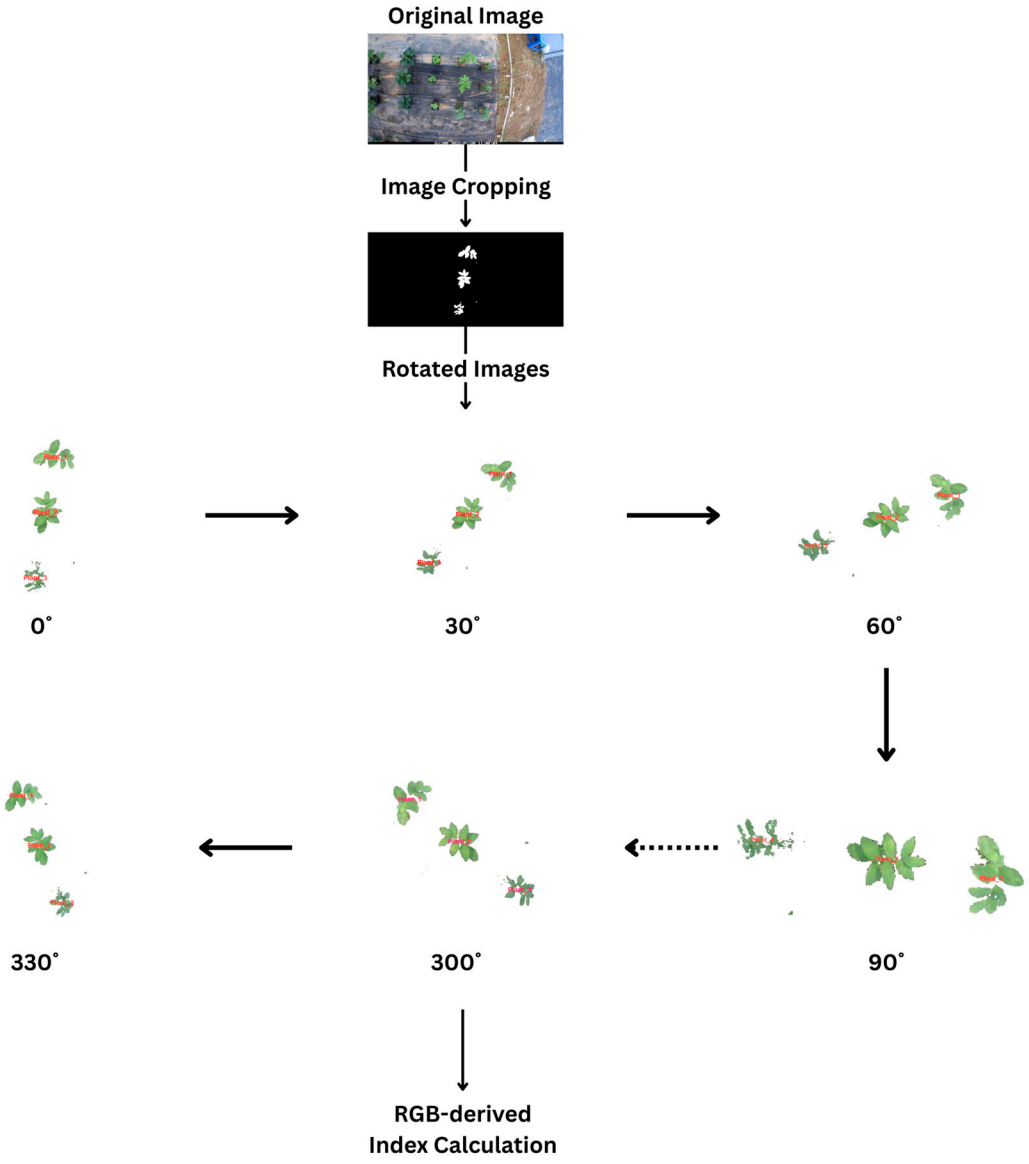

Figure 2. Workflow of RGB image preprocessing and RGB-derived variable extraction. The workflow illustrates the sequential procedures: (1) cropping the original RGB image to the experimental region of interest (ROI); (2) segmenting plant regions using *k*-means clustering followed by ROI-based spatial filtering to remove background noise; (3) identifying individual plant objects using connected-component labeling (represented by different color labels); (4) generating twelve rotated images (0–330°, 30° intervals) to minimize orientation bias; and (5) calculating RGB-derived variables from each rotated image, followed by IQR-based outlier removal and averaging to obtain sampling-date species-level values.

2.5. Relationship Analysis Between PSI and RGB-Derived Variables

The analytical dataset comprised 50 species-by-stage observations representing ten species measured at five sequential soil-moisture stages. Each observation paired one sampling-date species-level RGB value with the corresponding species-level mean PSI. The RGB and fluorescence values had already been aggregated across the three pots; therefore,

the pot-level measurements were not retained as directly paired repeated observations and were not treated as independent samples in this analysis.

Pearson correlations between PSI and each of the 11 RGB-derived variables were calculated using all 50 aggregated species-by-stage observations (n = 50) to describe the unadjusted relationships across the progressive-drying sequence. These correlations were descriptive and did not account for species or soil-moisture stage.

For each RGB variable, two linear models were subsequently fitted using the same 50 observations. The first model included the RGB variable and species as categorical fixed effects (PSI ~ RGB variable + species) to estimate the common association after accounting for baseline differences among species. The second model additionally included soil-moisture stage as a categorical fixed effect (PSI ~ RGB variable + species + soil-moisture stage) to determine whether the RGB variable explained variation in PSI beyond the progressive soil-moisture gradient shared by both measurements. The significance of the RGB-variable term was evaluated using Type II ANOVA. The additional contribution of each RGB variable was quantified by comparing the coefficient of determination of the full model with that of the corresponding reduced model containing species and soil-moisture stage only (ΔR^2). Because the five soil-moisture stages occurred sequentially during progressive drying, this model controlled for the shared stage structure but could not separate soil-moisture effects from concurrent temporal changes. Unadjusted scatterplots and fitted regression lines were used only to visualize the overall direction of the relationships and were not used as evidence of an association independent of soil-moisture stage.

Because individual pot identities were not preserved as directly paired RGB–PSI observations after species-level aggregation, a pot-level repeated-measures or random-effects model could not be fitted retrospectively. Accordingly, inference was restricted to the 50 species-by-stage observations, and this limitation was considered when interpreting the relationships between PSI and the RGB variables.

2.6. Development of the RGB-Based Photochemical Proxy

Partial least-squares regression (PLSR) was used to develop an RGB-based proxy for estimating PSI. PLSR was selected because it can accommodate multicollinearity among RGB-derived variables by projecting the predictors onto latent components that maximize their covariance with the response variable [59,60]. Model development and validation were conducted in R using the caret and pls packages.

Predictor selection and model validation were performed using a nested leave-one-species-out (LOSO) procedure. In each of the ten outer folds, all five observations from one species were withheld as the test set, while the 45 observations from the remaining nine species were used as the training set. All data-dependent steps—including Pearson screening, predictor standardization, selection of the number of PLS components, VIP calculation, and final model fitting—were conducted independently using only the data within each outer training fold. Within each outer training fold, Pearson correlations between PSI and the 11 candidate RGB variables were calculated, and variables with $p < 0.05$ were retained as predictors for the initial PLSR model. The retained predictors were centered and scaled using caret::preProcess() with the means and standard deviations calculated from the training data. The resulting preprocessing parameters were then applied to the corresponding test data.

The initial PLSR model was fitted using pls::plsr() with ten-segment cross-validation (validation = "CV"). The inner cross-validation segments were generated at the observation level within the outer training data and were not grouped by species. The number of latent components was selected using pls::selectNcomp(method = "onesigma"). Under this criterion, the model with the smallest number of components whose cross-validated

prediction error was within one standard error of the minimum was selected; a minimum of one component was imposed. VIP scores were calculated from the initial PLSR model using the components selected within the corresponding training fold. Variables with VIP > 1 were retained for the final PLSR model. The selected predictors were again centered and scaled using parameters estimated exclusively from the training data, and the number of components was determined independently using the same inner cross-validation and one-standard-error procedure. The fitted final model was subsequently applied to the completely held-out species. No information from the test species was used in predictor screening, preprocessing, component selection, VIP calculation, or model fitting.

Predictions from the ten outer LOSO folds were pooled, providing one completely out-of-fold prediction for each of the 50 observations. The overall R^2, RMSE, MAE, and Pearson correlation were calculated exclusively from these 50 pooled out-of-fold predic-tions and therefore represent aggregated nested-LOSO performance. These values were kept distinct from the apparent in-sample performance obtained from the subsequent complete-data refit reported in Appendix B. Fold-specific R^2, RMSE, and MAE were also calculated separately for each held-out species. Because each species-specific test fold contained only five observations, fold-specific R^2 values were treated as descriptive measures and were not used to support strong conclusions regarding individual species. A training-mean baseline was evaluated within the same outer LOSO structure. For each fold, the mean PSI of the 45 training observations was assigned as the predicted value for all five observations of the held-out species. The pooled baseline R^2, RMSE, and MAE were calculated and compared with those of the initial and final PLSR models. Calibration of the pooled initial and final LOSO predictions was evaluated by fitting separate linear regressions of predicted PSI on observed PSI. For each model, the calibration intercept and slope were used to evaluate systematic offset and compression of the predicted range, respectively. Mean bias was calculated as the mean difference between predicted and observed PSI.

Following completion of nested LOSO validation, an implementation-form proxy was refitted using the complete dataset and the five predictors consistently selected across the outer folds. Predictor standardization was based on the complete-data means and standard deviations, whereas PSI was used on its original centered PCA-score scale without additional standardization. This complete-data fit was used only to obtain the final prediction equation and implementation coefficients and was kept separate from the nested LOSO estimate of predictive performance. The prediction equation, intercept, standardized regression coefficients, and predictor means and standard deviations are provided in Appendix B. Performance calculated from the complete-data fit was regarded as apparent in-sample fit and was not used as evidence of generalization to unseen species.

The performance metrics were calculated as follows:

$$\text{Coefficient of determination } (R^2) = 1 - \frac{\Sigma(y_i - \hat{y}_i)^2}{\Sigma(y_i - \overline{y})^2} \quad (2)$$

$$\text{Root Mean Square Error (RMSE)} = \sqrt{\frac{1}{N}\Sigma(y_i - \hat{y}_i)^2} \quad (3)$$

$$\text{Mean Absolute Error (MAE)} = \frac{1}{N}\Sigma|(y_i - \hat{y}_i)| \quad (4)$$

where y_i is the observed value, $\hat{y}_i$ is the predicted value, $\overline{y}$ is the mean observed value, and N is the total number of observations.

2.7. Statistical Analysis

Statistical analyses were performed using R software (version 4.1.2) [61]. Differences in PSI among soil-moisture stages were evaluated using a species-adjusted fixed-effects model, with soil-moisture stage and species included as categorical fixed effects (PSI ~ soil-moisture stage + species). Species was included as a blocking factor to account for systematic differences among the ten species. The analytical unit was the species × soil-moisture-stage mean, resulting in 50 observations. Because the RGB and OJIP measurements were not directly paired at the individual-plant level and plant/pot identifiers were not retained after aggregation, a plant-level repeated-measures or nested random-effects structure could not be reconstructed from the analyzed dataset. The significance of each fixed effect was evaluated using Type II ANOVA, and effect sizes were reported as partial η^2. Species-adjusted estimated marginal means and their 95% confidence intervals were calculated for each soil-moisture stage, and pairwise comparisons were adjusted using Tukey's method. Model assumptions were evaluated using residual diagnostic plots, the Shapiro–Wilk test of residual normality, and Levene's test of homogeneity of variance. Statistical significance was determined at $p < 0.05$.

3. Results

3.1. Construction of the Photochemical Status Index (PSI)

PCA was performed using five JIP-test energy-flux variables (RC/CS, ABS/CS, TRo/CS, ET2o/CS, and RE1o/CS) to construct the PSI. The first principal component (PC1) explained 96.5% of the total variance, whereas the second principal component (PC2) explained 1.7% (Figure 3a). All five variables had similar negative loadings on PC1, ranging from −0.443 to −0.453 (Table 4). The high proportion of variance explained by PC1 therefore primarily reflected the strong covariance and mathematical relatedness among these JIP-test flux variables. Accordingly, PC1 was interpreted as a shared photochemical-flux axis rather than as evidence of coordination among multiple independent physiological systems. The PCA biplot showed a progressive shift in the samples from the negative to the positive direction of PC1 as soil moisture decreased. Following the sign-inversion procedure described in Section 2.3, the PC1 scores were converted to PSI values such that higher values represented greater maintenance of the measured photochemical fluxes, whereas lower values represented greater drought-associated photochemical impairment.

Species-specific trajectories showed that the direction of PSI change was broadly consistent across the ten species, with PSI generally declining as soil moisture decreased, although the magnitude and pattern of change varied among species (Figure 3b). Across species, PSI decreased progressively with declining soil moisture (Figure 3c). Each soil-moisture stage comprised ten species-by-stage observations, with one aggregated observation per species. After accounting for differences among species, soil-moisture stage had a significant effect on PSI ($F_{4,36} = 108.09$, $p < 2.2 \times 10^{-16}$, partial $\eta^2 = 0.92$), and the species effect was also significant ($F_{9,36} = 3.59$, $p = 0.00286$, partial $\eta^2 = 0.47$). The species-adjusted estimated marginal means of PSI were 2.867 (95% CI: 2.427–3.308), 1.333 (0.892–1.774), 0.272 (−0.169–0.713), −1.818 (−2.259 to −1.377), and −2.654 (−3.095 to −2.213) at soil-moisture stages of 31.0%, 21.5%, 7.4%, 6.1%, and 4.6%, respectively. Tukey-adjusted comparisons distinguished 31.0%, 21.5%, and 7.4% as separate groups, whereas PSI did not differ significantly between 6.1% and 4.6%. Residual diagnostics indicated no substantial violations of normality or homogeneity of variance (Shapiro–Wilk $W = 0.972$, $p = 0.285$; Levene's $F_{4,45} = 1.498$, $p = 0.219$). The constructed PSI was subsequently used as the reference photochemical variable in the RGB relationship and proxy-development analyses.

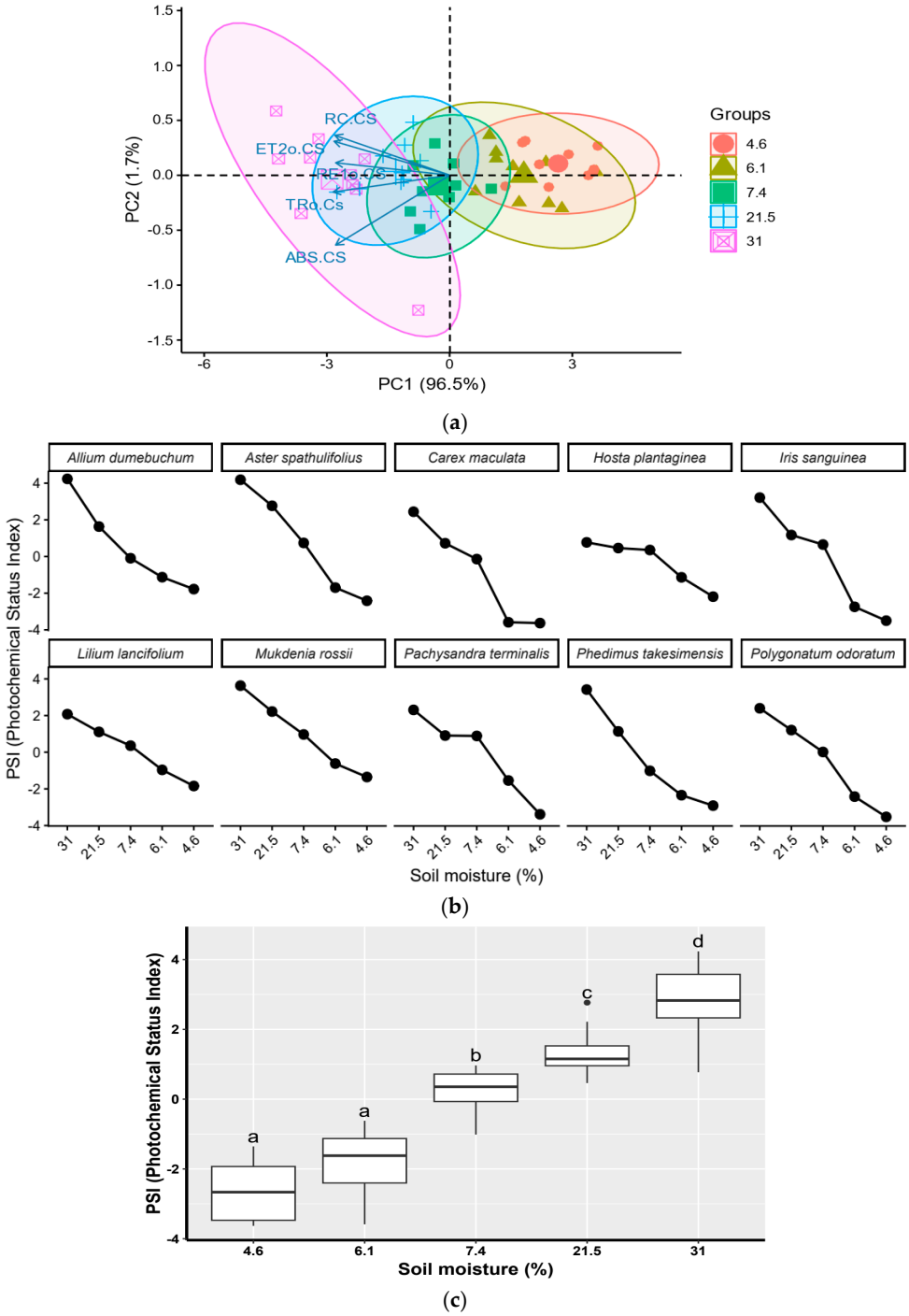

Figure 3. Construction and evaluation of the Photochemical Status Index (PSI) under progressive soil drying. (**a**) Principal component analysis (PCA) biplot based on five JIP-test energy-flux variables (RC/CS, ABS/CS, TRo/CS, ET2o/CS, and RE1o/CS) measured at five soil-moisture stages (31.0%, 21.5%, 7.4%, 6.1%, and 4.6%). Ellipses indicate the 95% confidence regions for each soil-moisture stage. (**b**) Species-specific trajectories of the sign-inverted PSI across the sequential soil-moisture stages. Each panel represents one species, and the connected points show its PSI values from the highest to the lowest soil-moisture stage. (**c**) Distribution of the sign-inverted PSI across soil-moisture stages. Different lowercase letters indicate significant differences among species-adjusted estimated marginal means based on Tukey-adjusted comparisons ($p < 0.05$).

Table 4. Means, standard deviations, and loadings of variables on principal component 1 (PC1) used to construct the Photochemical Status Index (PSI).

Parameter	Mean	Standard Deviation	PC1 Loading
RC/CS	10,572.76	6930.51	−0.447
ABS/CS	22,705.78	11,338.97	−0.443
TRo/CS	16,245.20	10,196.89	−0.453
ET2o/CS	9941.31	6700.99	−0.450
RE1o/CS	4398.24	2625.77	−0.443

Values are based on the 50 species-by-soil-moisture-stage observations used in the PCA. The means and standard deviations were used to standardize each variable before PCA. The loadings shown are the original PC1 loadings. PC1 scores were subsequently multiplied by −1 to construct the Photochemical Status Index (PSI), such that higher PSI values indicated greater maintenance of the measured photochemical fluxes.

3.2. Relationships Between PSI and RGB-Derived Variables

Pearson correlation analysis was used to descriptively summarize the unadjusted relationships between PSI and the 11 RGB-derived variables (Figure 4a). GLI, NGRDI, ExG, ExGR, and g were positively correlated with PSI, whereas BGI, ExR, and CIVE were negatively correlated with PSI ($p < 0.05$). VARI, r, and b did not show significant unadjusted correlations with PSI. The RGB-derived variables were also strongly intercorrelated. Several pairs had Pearson correlation coefficients close to ±1, including ExG and CIVE ($r \approx -1.00$), GLI and g ($r = 0.99$), BGI and b ($r = 0.97$), GLI and ExG ($r = 0.96$), and NGRDI and ExR ($r = -0.96$). These high correlations reflect the fact that the variables were derived from the same R, G, and B channels and, in several cases, were mathematically related transformations of largely overlapping color information. Accordingly, the individual indices should not be interpreted as independent physiological signals or ranked as representing distinct underlying processes.

The corresponding simple linear regressions showed broadly comparable moderate univariate associations for CIVE ($R^2 = 0.526$, $p < 0.001$), ExG ($R^2 = 0.517$, $p < 0.001$), and g ($R^2 = 0.475$, $p < 0.001$) (Figure 4b–l). The small numerical differences among these R^2 values were not interpreted as evidence that one variable performed better than the others, particularly given their strong intercorrelations and derivation from overlapping RGB information. The observations were also clearly structured by soil-moisture stage along the regression gradients.

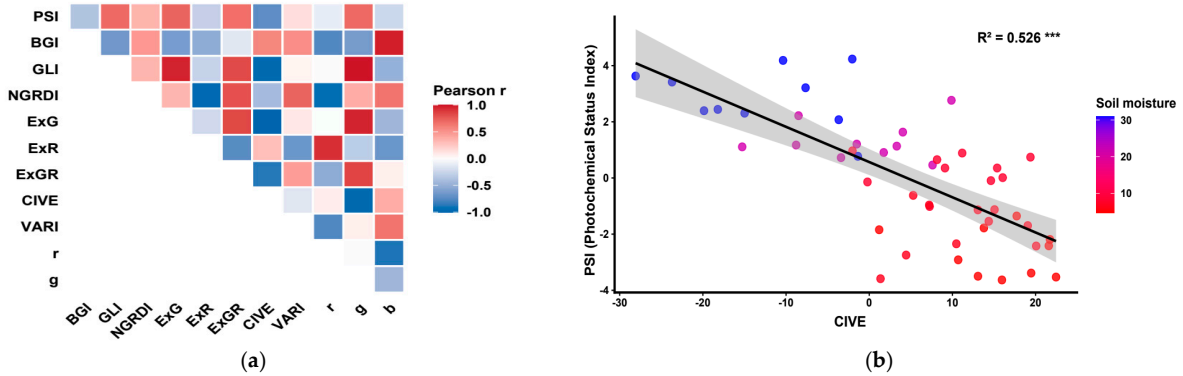

(**a**) (**b**)

Figure 4. *Cont.*

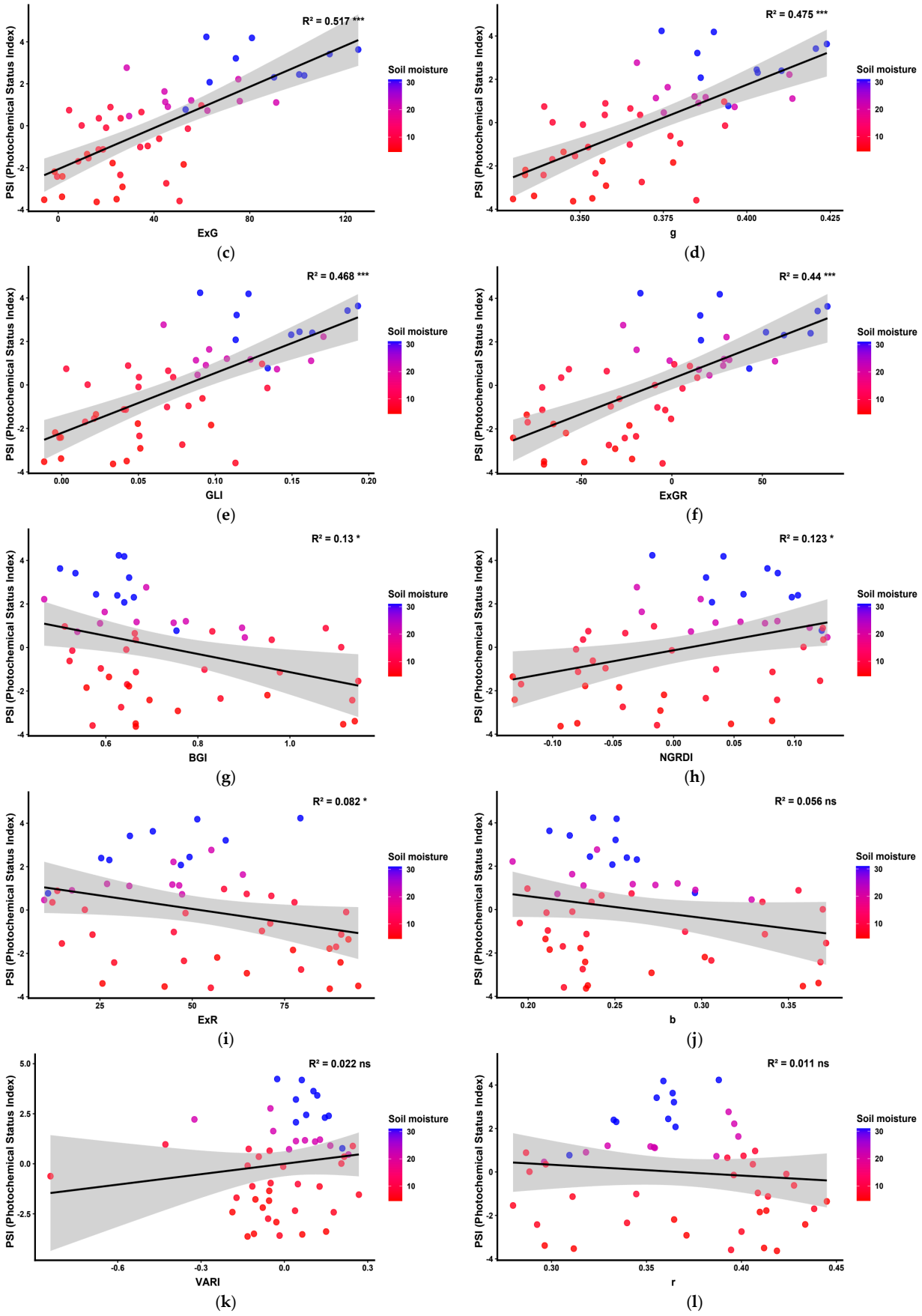

Figure 4. Unadjusted relationships between the Photochemical Status Index (PSI) and RGB-derived variables. (**a**) Heatmap of Pearson correlation coefficients among PSI and the 11 RGB-

derived variables based on 50 aggregated species-by-soil-moisture-stage observations (n = 50). Cell colors indicate the direction and magnitude of the correlations. (**b**–**l**) Simple linear regressions between PSI and CIVE, ExG, g, GLI, ExGR, BGI, NGRDI, ExR, b, VARI, and r, respectively. Point colors indicate soil-moisture stage. These analyses describe the overall associations across the progressive-drying sequence and do not represent relationships adjusted for species or soil-moisture stage. Significance codes are as follows: ns, not significant ($p \geq 0.05$); * $p < 0.05$; and *** $p < 0.001$.

After accounting for species, several RGB-derived variables remained significantly associated with PSI. However, when soil-moisture stage was additionally included as a categorical fixed effect, none of the 11 RGB-variable effects remained significant (all $p \geq 0.311$). Their incremental explanatory contributions beyond species and soil-moisture stage were also minimal, with ΔR^2 values ranging from < 0.001 to 0.0021; the largest increase was obtained for ExG (ΔR^2 = 0.0021). These results indicate that the unadjusted RGB–PSI relationships largely reflected shared variation along the sequential soil-moisture/time gradient rather than substantial RGB-associated variation independent of that gradient.

The full-dataset Pearson correlations shown in Figure 4 were used only to describe the unadjusted associations and were not used for global predictor selection. Predictor screening and VIP selection were conducted independently within each outer training fold of the nested LOSO procedure, and predictor-selection stability is reported in Section 3.3.

3.3. Development of the RGB-Based Photochemical Proxy

3.3.1. Development of the Initial RGB-Based Photochemical Proxy

The initial RGB-based photochemical proxy was developed using predictors that passed Pearson screening independently within each outer training fold of the nested LOSO procedure. Depending on the species withheld, seven or eight of the 11 candidate RGB-derived variables passed the screening criterion ($p < 0.05$). The number of latent components was subsequently selected by inner ten-segment cross-validation conducted independently within each outer training set. One component was selected for the initial PLSR model in each of the ten outer folds. This consistency refers to the component selected for each outer-fold model and not to selection within every individual inner cross-validation segment.

When the predictions for the completely held-out species were pooled across the ten outer folds, the initial model yielded an R^2 of 0.437, an RMSE of 1.632, and an MAE of 1.210 (Table 5). Observed and out-of-fold predicted PSI values were positively correlated (Pearson's r = 0.665; Figure 5). These results indicate that the initial model captured a moderate portion of the variation in PSI for species excluded from model development.

Prediction performance varied substantially among the held-out species (Table 6). The initial model showed relatively high descriptive R^2 values for *Mukdenia rossii* (0.959), *Hosta plantaginea* (0.866), *Polygonatum odoratum* (0.799), *Pachysandra terminalis* (0.736), and *Phedimus takesimensis* (0.671). In contrast, R^2 was close to zero for *Carex maculata* (0.012), *Allium dumebuchum* (−0.019), and *Aster spathulifolius* (0.042), and was negative for *Lilium lancifolium* (−0.168). The negative R^2 values indicate that, within these held-out species, the model performed worse than predictions based on the corresponding species-specific observed mean. Because each species-specific test fold contained only five observations, however, these fold-level metrics were interpreted descriptively.

Calibration analysis of the pooled predictions produced an intercept of 0.069, a slope of 0.486, and a mean bias of 0.069. Although the small intercept and mean bias indicated little overall systematic offset, the slope substantially below 1 showed that predictions were compressed toward the center of the PSI range. Accordingly, low observed PSI values tended to be overpredicted, whereas high observed values tended to be underpredicted (Figure 5).

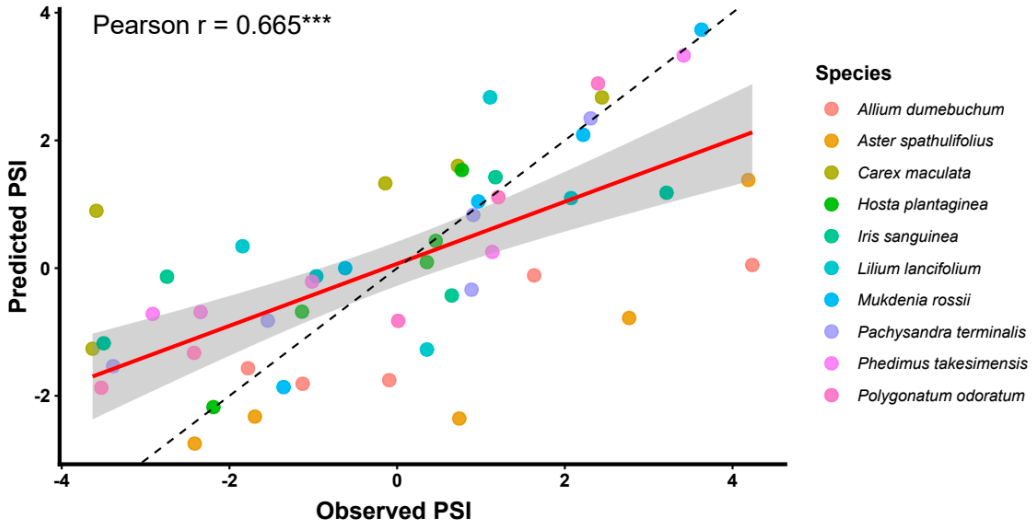

Figure 5. Observed and out-of-fold predicted Photochemical Status Index (PSI) values from the initial PLSR model under nested leave-one-species-out validation. Each point represents one species-by-soil-moisture-stage observation, and colors indicate the held-out species. The dashed black line denotes the 1:1 relationship, whereas the solid red line and shaded band represent the fitted regression and its 95% confidence interval, respectively. The pooled out-of-fold predictions were positively correlated with the observed PSI values (Pearson's $r = 0.665$). The calibration regression had an intercept of 0.069 and a slope of 0.486, with a mean bias of 0.069. The slope substantially below 1 indicates compression of predictions toward the center of the observed PSI range. Significance codes are as follows: *** $p < 0.001$.

Table 5. Pooled predictive performance and calibration of the nested leave-one-species-out models.

Model	R^2	RMSE	MAE	Pearson *r*	Calibration Intercept	Calibration Slope	Mean Bias
Training-mean baseline	−0.015	2.191	1.843	-	-	-	-
Initial PLSR	0.437	1.632	1.210	0.665	0.069	0.486	0.069
Final PLSR	0.469	1.585	1.183	0.687	−0.003	0.509	−0.003

Performance was calculated from the 50 pooled out-of-fold predictions. The training-mean baseline assigned the mean PSI of each outer training set to the five observations of the corresponding held-out species. Calibration was evaluated by regressing predicted PSI on observed PSI.

Table 6. Fold-specific performance of the initial and final PLSR models under nested leave-one-species-out validation.

Species	Predictors (n)		Components		R^2 (Initial)	R^2 (Final)	RMSE (Initial)	RMSE (Final)	MAE (Initial)	MAE (Final)
	Initial	Final	Initial	Final						
Polygonatum odoratum	7	5	1	1	0.799	0.832	0.990	0.905	0.836	0.793
Carex maculata	8	5	1	1	0.012	0.098	2.396	2.289	1.886	1.779
Pachysandra terminalis	8	5	1	1	0.736	0.754	1.044	1.008	0.782	0.762
Hosta plantaginea	8	5	1	1	0.866	0.883	0.414	0.388	0.305	0.342
Lilium lancifolium	7	5	1	1	−0.168	−0.179	1.519	1.526	1.439	1.446
Allium dumebuchum	8	5	1	1	−0.019	0.103	2.184	2.049	1.698	1.592
Iris sanguinea	7	5	1	1	0.444	0.450	1.875	1.865	1.660	1.656
Phedimus takesimensis	7	5	1	1	0.671	0.673	1.342	1.338	1.126	1.116
Aster spathulifolius	7	5	1	1	0.042	0.062	2.472	2.445	2.082	2.049
Mukdenia rossii	7	5	1	1	0.959	0.959	0.368	0.369	0.288	0.300

Each outer fold contained 45 training observations and five test observations from the held-out species. Fold-specific metrics are descriptive because each test fold contained only five observations. The final model used g, GLI, ExG, ExGR, and CIVE in all folds.

3.3.2. Predictor Selection and Stability Based on VIP Scores

VIP scores were calculated independently from the initial PLSR model within each outer training fold. Because the preceding Pearson screening was also repeated within each fold, the variables available for VIP evaluation differed slightly among folds. The variables g, GLI, NGRDI, ExG, ExGR, and CIVE were available in all ten folds, whereas BGI, ExR, and b were available in nine, four, and one fold, respectively.

Five variables were consistently retained using the VIP > 1 criterion in all ten outer folds: CIVE (mean VIP = 1.19, SD = 0.023), ExG (1.18, 0.025), g (1.13, 0.030), GLI (1.13, 0.033), and ExGR (1.09, 0.042) (Figure 6). Thus, each of these variables had a selection frequency of 100%. In contrast, NGRDI had a mean VIP of 0.58 (SD = 0.067) across the ten folds in which it was available and was not selected in any fold. BGI, ExR, and b also remained below the selection threshold in all folds in which they were available, with mean VIP scores of 0.60, 0.56, and 0.49, respectively. Because b was available in only one fold, an SD was not calculated for this variable.

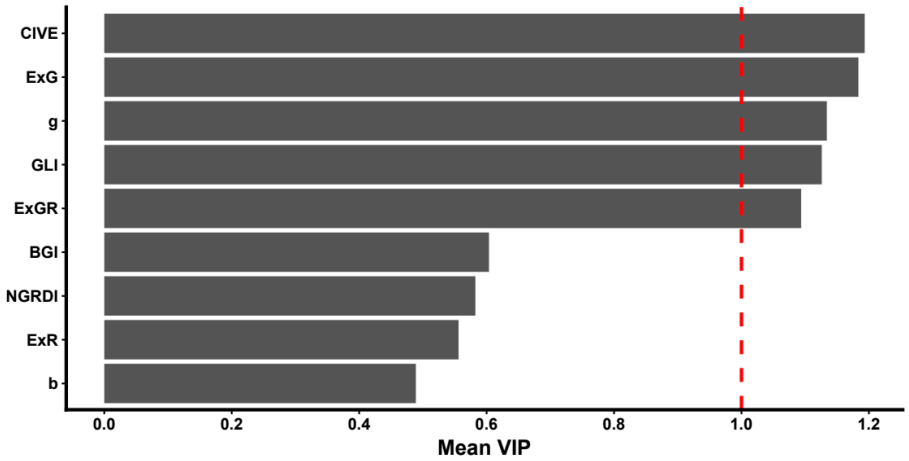

Figure 6. Mean variable importance in projection (VIP) scores across the nested leave-one-species-out folds. Bars represent the mean VIP scores calculated across the outer training folds in which each variable passed the preceding Pearson screening step and was therefore available to the initial PLSR model. The dashed red line indicates the VIP selection threshold of 1.0. CIVE, ExG, g, GLI, and ExGR exceeded this threshold and were retained in all ten outer folds. The numbers of folds in which the remaining variables were available were nine for BGI, ten for NGRDI, four for ExR, and one for b; none of these variables exceeded the threshold in any available fold.

Accordingly, the predictor set was reduced to g, GLI, ExG, ExGR, and CIVE for the final PLSR model. The identical selection of these five variables across all outer folds indicated stable predictor selection under the nested LOSO procedure, despite the high correlations among several RGB-derived variables.

3.3.3. Development of the Final RGB-Based Photochemical Proxy

The final RGB-based photochemical proxy was developed using g, GLI, ExG, ExGR, and CIVE, which were retained in all ten outer folds. Predictor preprocessing, component selection, model fitting, and prediction were conducted independently within each outer training fold. As in the initial model, one latent component was selected for the final PLSR model in every outer fold (Table 6).

The primary estimate of predictive performance was obtained from the pooled out-of-fold predictions of the final model under nested LOSO validation. The final model yielded an aggregated LOSO R^2 of 0.469, an RMSE of 1.585, an MAE of 1.183, and a Pearson correlation of 0.687 between observed and predicted PSI (Table 5). Accordingly,

R^2 = 0.469 was treated as the main estimate of the model's predictive ability for previously unseen species. The corresponding aggregated LOSO R^2 of the initial model was 0.437 and was reported only as a model-development comparison. The similar performance of the two models indicated that restricting the final model to five consistently selected predictors improved parsimony without materially reducing predictive performance. Thus, the main advantage of the final model was the reduction from seven or eight fold-dependent predictors to a stable set of five predictors rather than evidence of a robust improvement in predictive accuracy. The training-mean baseline evaluated under the same outer LOSO structure yielded an R^2 of −0.015, an RMSE of 2.191, and an MAE of 1.843 (Table 5). Relative to this baseline, the final model reduced RMSE by 27.7% and MAE by 35.8%, indicating that the RGB-based model provided predictive information beyond the mean PSI of the corresponding outer training set. Nevertheless, the final model captured only a moderate portion of the pooled out-of-species variation.

Performance remained strongly heterogeneous among the held-out species (Table 6). Relatively high descriptive R^2 values were obtained for *Mukdenia rossii* (0.959), *Hosta plantaginea* (0.883), *Polygonatum odoratum* (0.832), *Pachysandra terminalis* (0.754), and *Phedimus takesimensis* (0.673). In contrast, performance was weak for *Carex maculata* (R^2 = 0.098), *Allium dumebuchum* (0.103), and *Aster spathulifolius* (0.062). The R^2 for *Lilium lancifolium* was negative (−0.179), indicating worse performance than prediction based on the observed mean for that species. These species-level results, although descriptive because each fold contained only five observations, demonstrate that predictive performance did not generalize uniformly across all evaluated species.

Calibration of the pooled final-model predictions produced an intercept of −0.003, a slope of 0.509, and a mean bias of −0.003. The near-zero intercept and mean bias indicated little overall systematic offset. However, the slope substantially below 1 indicated compression of the predicted values toward the center of the observed PSI range. The observed PSI values ranged from −3.632 to 4.235, whereas the corresponding predictions ranged from −2.707 to 3.800. Consequently, severely impaired photochemical states tended to be overpredicted, while states with high maintenance of photochemical fluxes tended to be underpredicted (Figure 7). Following nested LOSO validation, the final proxy was refitted using the complete dataset and the five consistently selected predictors to obtain an implementation equation. This complete-data fit yielded an apparent R^2 of 0.519, an RMSE of 1.509, and an MAE of 1.117. These values represent in-sample fit and were not interpreted as estimates of performance for unseen species. The final equation, regression coefficients, and predictor standardization parameters are provided in Appendix B.

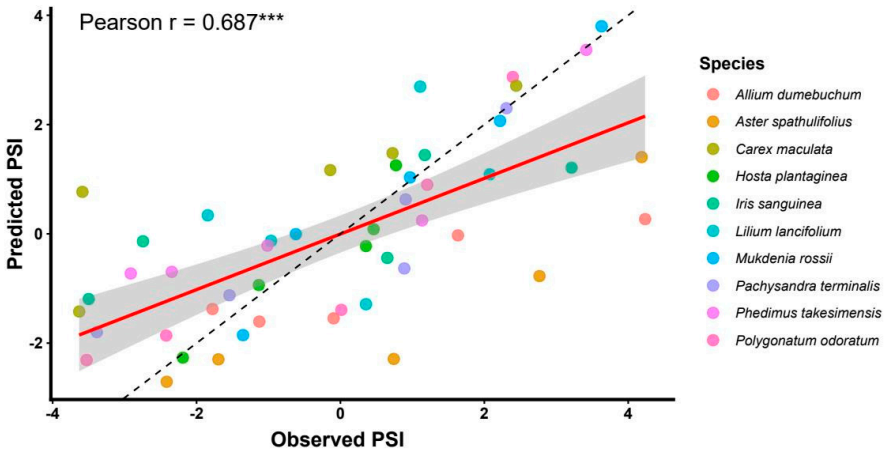

Figure 7. Observed and out-of-fold predicted Photochemical Status Index (PSI) values from the final PLSR model under nested leave-one-species-out validation. Each point represents one species-by-soil-

moisture-stage observation, and colors indicate the held-out species. The dashed black line denotes the 1:1 relationship, whereas the solid red line and shaded band represent the fitted regression and its 95% confidence interval, respectively. The pooled out-of-fold predictions were positively correlated with the observed PSI values (Pearson's r = 0.687). The calibration regression had an intercept of −0.003 and a slope of 0.509, with a mean bias of −0.003. Although the mean bias was negligible, the slope substantially below 1 indicates that low PSI values tended to be overpredicted and high PSI values tended to be underpredicted. Significance codes are as follows: *** $p < 0.001$.

4. Discussion

4.1. Photochemical Interpretation of the PSI

Chlorophyll fluorescence analysis is widely recognized as a sensitive approach for detecting plant responses to environmental stress because it provides information on the functional status of photosystem II (PSII) and photosynthetic energy conversion [17,30,62–64]. Among fluorescence techniques, OJIP transient analysis enables the characterization of energy absorption, excitation-energy trapping, electron transport, and the reduction in terminal electron acceptors [65–67]. However, the JIP-test flux variables describing these processes are strongly interrelated and are partly connected through their mathematical definitions and shared underlying fluorescence measurements [68]. Their integration must therefore be interpreted as a summary of shared variation within the chlorophyll-fluorescence and photochemical domain rather than as integration of independent dimensions of whole-plant physiology.

In the present study, PCA was used to summarize the common variation among five pre-selected JIP-test energy-flux variables—RC/CS, ABS/CS, TRo/CS, ET2o/CS, and RE1o/CS—into a single Photochemical Status Index (PSI). PCA provides a means of reducing dimensionality while retaining the dominant pattern of variation among correlated variables [69,70]. PC1 explained 96.5% of the total variance, and the five variables had similar loadings. This high explained variance primarily reflected the use of a pre-selected set of strongly covarying and mathematically related variables from the same JIP-test measurement domain, rather than demonstrating coordinated regulation across multiple independent physiological systems. Accordingly, PSI was interpreted as a chlorophyll-fluorescence-based photochemical status index representing the shared variation in the measured energy fluxes.

After accounting for species differences, PSI declined markedly across the sequential soil-moisture stages, although the two lowest moisture stages did not differ significantly. This pattern indicates that PSI was responsive to the photochemical changes accompanying progressive soil drying in the present experiment. However, PSI was constructed exclusively from fluorescence-derived variables measured within the same dataset and was not validated against an independent physiological reference such as leaf water potential, stomatal conductance, carbon assimilation, respiration, or biochemical stress markers. It should therefore be regarded as a fluorescence-referenced descriptor of photochemical status rather than a measure of overall plant physiological condition. Within this defined scope, PSI provided the reference variable for evaluating whether visible RGB information could approximate variation in the measured photochemical fluxes.

4.2. Interpretation of the Relationships Between PSI and RGB-Derived Variables

Drought can alter visible leaf and canopy characteristics through multiple, potentially overlapping processes, including changes in pigment composition, tissue water content, leaf structure, senescence, and canopy architecture [71–75]. Such changes may affect the relative red, green, and blue signals recorded by conventional cameras [38,40,76]. However,

chlorophyll, carotenoids, anthocyanins, leaf water content, and leaf optical properties were not measured in the present study. Consequently, these processes provide plausible hypotheses for the observed RGB responses but cannot be identified as the mechanisms underlying the relationships with PSI.

The unadjusted analyses showed moderate relationships between several RGB-derived variables and PSI. Greenness-related variables, including GLI, ExG, NGRDI, ExGR, and g, were positively associated with PSI, whereas CIVE, ExR, and BGI showed negative associations. CIVE, ExG, and g showed broadly comparable moderate univariate associations with PSI, with R^2 values of 0.526, 0.517, and 0.475, respectively. Given their strong intercorrelations and derivation from overlapping RGB channel information, these small numerical differences were not interpreted as a meaningful ranking among the variables. These associations indicate that variation in visible RGB information accompanied variation in the fluorescence-derived PSI. Previous studies have related greenness-based RGB variables to chlorophyll abundance and vegetation vigor [77,78]; however, the present associations do not demonstrate that any particular variable directly measured chlorophyll abundance, pigment degradation, leaf water status, or a specific photochemical process. Accordingly, the present results do not demonstrate that any of these variables captured a broader or more distinct physiological signal than the others. CIVE and the other RGB-derived variables are mathematical transformations of visible color information, and their responses can also be influenced by illumination, camera characteristics, leaf orientation, canopy structure, background separation, and species-specific optical properties. Direct measurements of pigments, tissue water content, and spectral reflectance would be required to determine the biological and optical mechanisms responsible for these relationships.

An important qualification is that both PSI and the RGB-derived variables were strongly structured along the sequential soil-moisture stages. After species differences were accounted for, several RGB-derived variables remained associated with PSI. However, after soil-moisture stage was additionally included in the models, these associations were markedly attenuated, and the incremental explanatory contribution of the RGB-derived variables was minimal, with a maximum increase in R^2 of approximately 0.002. Because soil moisture declined sequentially over time, the effects of soil drying cannot be separated fully from concurrent temporal changes such as plant development, acclimation, or canopy modification in the present dataset. The observed RGB–PSI relationships should therefore be interpreted primarily as shared responses along the soil-moisture/time gradient rather than as evidence that RGB imagery captured substantial photochemical variation independently of that gradient.

Previous studies have related RGB-derived variables to chlorophyll content, leaf water status, and photosynthetic characteristics [79–82]. The present findings are compatible with the possibility that visible canopy information can serve as a low-cost correlate of fluorescence-derived photochemical status under progressive drying. However, they do not extend RGB imagery to assessment of overall plant physiological condition, nor do they demonstrate incremental physiological information independent of soil moisture and time. Establishing such capability would require independent temporal controls, direct measurement of the proposed pigment and water-status mechanisms, and validation against physiological variables that were not used to construct PSI.

4.3. Interpretation of the RGB-Based Photochemical Proxy

Chlorophyll fluorescence analysis provides sensitive information about plant photochemical responses, but its use can be constrained by the need for specialized instrumentation, measurement protocols, and relatively low throughput [83,84]. These constraints motivate the development of image-based approaches that can provide approximate infor-

mation on plant status using readily obtainable RGB images for phenotyping and precision horticulture [85,86]. Within this context, the RGB-based proxy developed in the present study should not be regarded as a replacement for chlorophyll fluorescence measurements or as a direct measurement of photosynthetic electron transport. Rather, it is a fluorescence-referenced surrogate designed to estimate variation in the PSI from visible canopy characteristics.

The primary estimate of predictive performance was obtained from the nested LOSO validation, in which all predictor screening, preprocessing, component selection, VIP calculation, and model fitting were conducted without information from the held-out species. The final model yielded a pooled out-of-fold R^2 of 0.469, an RMSE of 1.585, and an MAE of 1.183. Thus, the five-variable model captured a moderate portion of PSI variation in species excluded from model development. The final model also outperformed the training-mean baseline, which yielded an R^2 of −0.015, an RMSE of 2.191, and an MAE of 1.843. Relative to this baseline, the final model reduced RMSE by 27.7% and MAE by 35.8%. These results indicate that the RGB-derived variables contained predictive information about PSI beyond the mean of the corresponding outer training set, but they do not demonstrate precise or uniform prediction across species.

The final model had performance comparable to that of the initial model while using fewer predictors. The initial model produced an R^2 of 0.437, an RMSE of 1.632, and an MAE of 1.210, whereas the final model produced an R^2 of 0.469, an RMSE of 1.585, and an MAE of 1.183. Because the differences were small and were not accompanied by an uncertainty-based comparison, they were not interpreted as a robust improvement in predictive accuracy. Instead, the main benefit of VIP selection was parsimony and selection stability: g, GLI, ExG, ExGR, and CIVE were retained in all ten outer folds despite the high correlations among several RGB-derived variables.

Published RGB-based studies have reported varying predictive performance depending on the target variable, species scope, experimental conditions, and validation design. Ref. [36] reported R^2 values exceeding 0.70 for most regressions using ExG, VARI, or g to estimate Fv/Fm, NDVI, and PRI in wheat and pea under drought or salinity. However, those regressions were developed separately for each species and stress condition using treatment- and time-point-averaged values and did not evaluate transferability to a completely held-out species. In RGB-based SPAD estimation for Hopea hainanensis, ref. [77] reported independent-test R^2 values of 0.306–0.377 without inclusion of the shade condition and 0.577–0.785 when shade was included as an additional predictor. Against this context, the nested-LOSO R^2 of 0.469 obtained in the present study indicates moderate predictive performance under the more demanding task of transferring the model to species excluded entirely from model development. Nevertheless, direct numerical comparisons should be interpreted cautiously because the studies differed in their physiological targets, plant material, experimental covariates, and validation procedures.

Calibration analysis further qualified model performance. For the final model, the calibration intercept and mean bias were close to zero (−0.003 for both), but the calibration slope was 0.509. This slope indicates substantial compression toward the center of the PSI range: low PSI values associated with greater photochemical impairment tended to be overpredicted, whereas high PSI values associated with greater maintenance of the measured photochemical fluxes tended to be underpredicted. The proxy may therefore be less reliable for distinguishing the most severely impaired and the highest photochemical states, even when its average bias across the complete set of out-of-fold predictions is small.

After nested validation, the model was refitted to the complete dataset solely to derive the final implementation equation and standardization parameters presented in Appendix B. The apparent complete-data R^2 of 0.519 was not used as evidence of predictive

performance or generalization to unseen species. Accordingly, the contribution of the proposed framework lies in demonstrating that inexpensive RGB imagery can provide a moderate, fluorescence-referenced approximation of the PSI under the conditions examined, while its predictive range and domain of applicability remain limited.

4.4. Applicability and Limitations of the RGB-Based Photochemical Proxy

Nested LOSO validation provided a direct assessment of prediction for species excluded from model development, but performance varied substantially among the ten held-out species. The final model showed relatively high descriptive R^2 values for several species, whereas performance was weak and close to zero for *Carex maculata*, *Allium dumebuchum*, and *Aster spathulifolius*, and negative for *Lilium lancifolium*. These results indicate that the relationship between visible RGB characteristics and PSI did not generalize uniformly across the evaluated species. The proposed proxy should therefore be interpreted as a preliminary approach for approximating shared photochemical trends under the conditions studied rather than as a universally applicable predictor with equivalent accuracy across ornamental species.

Species-dependent responses of RGB characteristics to water stress have also been reported in other ornamental plants. A previous study [76] found markedly different color responses among three urban shrub species subjected to contrasting irrigation conditions: extreme drought reduced the green color coordinate of *Euonymus japonicus* by approximately 40% and the red color coordinate of *Berberis thunbergii* var. atropurpurea by approximately 35%, whereas the color indices of *Ligustrum* × *vicaryi* remained comparatively stable, with variation below 15%. The relationship between soil water content and the corresponding color index also differed among species. These findings indicate that the same water-stress conditions can produce substantially different visible-color responses depending on species, supporting the expectation that a single RGB-to-photochemical-status relationship may not transfer uniformly across different species. However, that study evaluated species-specific color responses rather than held-out-species predictive performance and therefore provides contextual support rather than external validation of the present model.

Biological differences may contribute to this heterogeneity. Species can differ in leaf morphology, canopy architecture, background exposure, surface properties, pigmentation, and the extent to which photochemical impairment is accompanied by visible change. However, these traits were not quantified in the present experiment, and their contributions cannot be distinguished from statistical and experimental sources of variation. Morphological or pigment-based explanations should therefore be considered hypotheses rather than demonstrated mechanisms.

Several statistical factors also limit the interpretation of species-specific performance. Each held-out species contained only five aggregated species-by-soil-moisture-stage observations, making fold-specific R^2 values sensitive to individual prediction errors and to the limited within-species PSI range. Aggregation removed information on variation among pots or individual plants and prevented plant-level random effects from being modeled. Differences in baseline PSI and RGB characteristics among species may also have produced offsets that could not be estimated for a completely unseen species. In addition, the calibration slope of 0.509 showed substantial shrinkage toward the center of the PSI range, limiting prediction at extreme photochemical states. Predictor screening and VIP selection could have caused information leakage if performed before cross-validation; in the revised analysis, this risk was addressed by repeating all selection and preprocessing steps exclusively within each outer training fold. Nevertheless, the small number of species

and observations limits the precision with which model complexity, selection stability, and out-of-species performance can be estimated.

The experimental design imposes further constraints. The five soil-moisture stages occurred sequentially during progressive drying and were consequently confounded with time. Without an independent well-watered temporal control measured at the corresponding sampling times, changes associated with soil drying could not be separated fully from plant development, acclimation, senescence, or temporal changes in canopy structure. The marked attenuation of RGB–PSI associations after adjustment for soil-moisture stage indicates that much of their relationship followed this common soil-moisture/time gradient. Consequently, the present analysis does not demonstrate that the RGB variables captured substantial within-condition photochemical variation independently of drought progression.

Limitations also arise from image acquisition and processing. Conventional RGB values depend on illumination, camera exposure and radiometric response, viewing geometry, and background conditions. Greenhouse illumination and camera radiometry were not independently calibrated using color or reflectance standards, which restricts transferability across imaging systems and environments. Automated segmentation may also become less reliable as leaves senesce, change color, overlap, or expose more background, and segmentation accuracy was not validated against manually annotated masks across all stress stages. The 12 rotated image outputs were averaged to produce a single observation and were not treated as independent biological replicates; therefore, they did not increase the effective sample size. This averaging avoided direct pseudo-replication but cannot substitute for independent biological replication, and its robustness should be evaluated under other canopy forms and imaging conditions.

Finally, the proxy was developed from 50 aggregated observations representing ten species from a single progressive-drought experiment. The same experiment supplied both the fluorescence variables used to construct PSI and the RGB information used to model it, although nested LOSO separated species during model development and testing. No external validation was conducted in a different greenhouse, season, camera system, experiment, or independent set of species. The complete-data equation in Appendix B should therefore be regarded as an implementation form specific to the present dataset rather than as a universally calibrated model.

Future studies should incorporate independent well-watered temporal controls, plant-level paired observations, direct measurements of pigments, water status, gas exchange, morphology, and optical properties, standardized illumination and radiometric references, and independent segmentation validation. External testing across seasons, facilities, cameras, and previously unrepresented species will be required to determine whether the proxy retains calibration and predictive value beyond the present experiment. Within these limitations, the current study provides an initial fluorescence-referenced framework for investigating whether low-cost RGB imagery can approximate variation in chlorophyll-fluorescence-derived photochemical status.

5. Conclusions

This study provides proof-of-concept evidence that RGB-derived variables can be used to approximate a chlorophyll-fluorescence-derived photochemical status gradient during progressive soil drying. The PSI summarized the shared variation among five highly correlated JIP-test energy-flux variables and should therefore be interpreted as an integrated chlorophyll-fluorescence-based photochemical status index rather than as a measure of overall plant physiological condition. Five RGB-derived predictors—g, GLI, ExG, ExGR, and CIVE—were retained in all ten outer folds, demonstrating stable predictor selection under the nested LOSO procedure.

For species excluded from model development, the final five-variable PLSR model achieved a pooled out-of-fold R^2 of 0.469, an RMSE of 1.585, and an MAE of 1.183. The model outperformed the training-mean baseline but captured only a moderate portion of out-of-species PSI variation. Performance varied substantially among species, and calibration analysis revealed compression of predictions toward the center of the PSI range, limiting discrimination of severely impaired and high photochemical states. Moreover, much of the observed RGB–PSI relationship followed the common sequential soil-moisture/time gradient, and the present experiment did not establish that RGB information captured substantial photochemical variation independently of that gradient.

Accordingly, the proposed proxy should be regarded as a fluorescence-referenced proof-of-concept framework rather than a deployment-ready or universally transferable model. Its principal contribution is the development and nested out-of-species evaluation of a low-cost RGB approach for approximating variation in fluorescence-derived photochemical status, together with an explicit characterization of its limitations. External validation using independent experiments, temporal controls, plant-level paired observations, standardized imaging conditions, additional seasons and greenhouses, different camera systems, and previously unrepresented species will be required before practical application.

Author Contributions: Conceptualization, S.J.L. and S.Y.Y.; methodology, S.J.L.; software, S.J.L.; validation, S.J.L., T.S.E. and S.Y.Y.; investigation, S.J.L. and T.S.E.; data curation, S.J.L.; writing—original draft preparation, S.J.L.; writing—review and editing, T.W.K. and S.Y.Y.; visualization, S.J.L.; supervision, T.W.K. and S.Y.Y.; project administration, T.W.K. and S.Y.Y.; funding acquisition, T.W.K. and S.Y.Y. All authors have read and agreed to the published version of the manuscript.

Funding: This study was supported by the Korea Institute of Planning and Evaluation for Technology in Food, Agriculture and Forestry (IPET) through the Agriculture and Food Convergence Technologies Program for Research Manpower development, funded by the Ministry of Agriculture, Food and Rural Affairs (MAFRA) (RS-2024-00400922).

Data Availability Statement: Data will be made available on request.

Acknowledgments: During the preparation of this manuscript, OpenAI ChatGPT (GPT-5.5) was used to assist with English language editing, grammar correction, sentence restructuring, and improvement of manuscript readability. The AI tool was not used to generate, analyze, or interpret scientific data, perform statistical analyses, develop the study design, or draw scientific conclusions. All study conception, experimental work, data analysis, interpretation of the results, and final manuscript revisions were performed and verified by the authors. The authors carefully reviewed and edited all AI-assisted output and accept full responsibility for the content of this manuscript.

Conflicts of Interest: The authors declare no conflicts of interest.

Abbreviations

The following abbreviations are used in this manuscript:

b	Normalized Blue
BGI	Blue Green Pigment Index
CIVE	Color Index of Vegetation Extraction
ExG	Excess Green Index
ExGR	Excess Green minus Excess Red Index
ExR	Excess Red Index
g	Normalized Green
GLI	Green Leaf Index
LOSO	Leave-One-Species-Out
NGRDI	Normalized Green Red Difference Index

OJIP	Chlorophyll fluorescence transient
PCA	Principal Component Analysis
PLSR	Partial Least Squares Regression
PSI	Photochemical Status Index
r	Normalized Red
VARI	Visible Atmospherically Resistant Index
VIP	Variable Importance in Projection

Appendix A. Sensitivity of RGB-Variable Outputs to Image Orientation

The sensitivity analysis quantified variation in segmentation-derived RGB-index outputs among the 12 in-plane orientations. Measurable orientation-dependent variation was observed for all 11 RGB variables, and the unrotated (0°) outputs differed from their corresponding 12-orientation means (Table A1). These results indicate that an estimate obtained from a single arbitrarily selected orientation did not necessarily represent the orientation-averaged output. Orientation averaging was therefore used to reduce the dependence of the final image-level estimates on any single image orientation. This analysis does not demonstrate improved segmentation accuracy or predictive performance.

Table A1. Sensitivity of segmentation-derived RGB-variable outputs to in-plane image orientation.

Index	Orientation-Specific SD, Median (IQR)	Orientation-Specific Range, Median (IQR)	Absolute Difference Between 0° Output and 12-Orientation Mean, Median (IQR)
BGI	0.0425 (0.0271–0.0779)	0.1340 (0.0862–0.2599)	0.0308 (0.0125–0.0530)
GLI	0.0190 (0.0112–0.0303)	0.0622 (0.0357–0.0995)	0.0120 (0.0053–0.0224)
NGRDI	0.0166 (0.0073–0.0301)	0.0542 (0.0234–0.0985)	0.0098 (0.0036–0.0197)
ExG	10.1508 (5.9092–15.6376)	33.2299 (18.4187–50.7828)	5.3593 (2.1494–9.7107)
ExR	5.7180 (2.7303–11.2201)	19.0123 (8.4426–36.6779)	3.6038 (1.3846–8.9286)
ExGR	13.6177 (7.2862–22.8995)	44.8713 (23.9510–75.2886)	8.4988 (3.1657–15.9659)
CIVE	4.0116 (2.2866–6.2211)	13.0235 (7.2732–20.5436)	2.1683 (0.8785–3.8678)
VARI	0.0271 (0.0098–0.0492)	0.0909 (0.0310–0.1594)	0.0112 (0.0038–0.0298)
r	0.0090 (0.0040–0.0159)	0.0300 (0.0122–0.0506)	0.0043 (0.0019–0.0099)
g	0.0090 (0.0053–0.0137)	0.0293 (0.0167–0.0452)	0.0056 (0.0024–0.0100)
b	0.0114 (0.0075–0.0187)	0.0359 (0.0238–0.0626)	0.0077 (0.0035–0.0133)

Values were calculated from 1369 source images representing all ten species for which valid outputs were available for all 12 orientations and all 11 RGB variables. Within each source image and orientation, outputs from all detected plant regions were first averaged. The orientation-specific SD and range were calculated across the resulting 12 orientation-level means. The absolute difference was calculated between the unrotated (0°) output and the corresponding mean of all 12 orientations. Values in the table are medians, with the first and third quartiles shown in parentheses. Because the RGB variables have different numerical scales, their absolute variability values should not be compared directly among variables. IQR, interquartile range; SD, standard deviation.

Appendix B. Final RGB-Based Photochemical Proxy

Following completion of the nested LOSO validation, the RGB-based photochemical proxy was refitted using the complete dataset of 50 species–stage observations. The five predictors that were consistently selected in all ten outer LOSO folds—g, GLI, ExG, ExGR, and CIVE—were used with one PLS component. This complete-data model was constructed to provide an implementation equation and was not used to estimate predictive performance for unseen species. Predictive performance was evaluated exclusively from the pooled out-of-fold predictions generated by nested LOSO validation and reported in the main text ($R^2 = 0.469$).

Before model fitting, each predictor was standardized using its complete-data mean and sample standard deviation:

$$z_j = \left(x_j - \overline{x}_j\right)/s_j \quad \text{(A1)}$$

where x_j is the observed value of predictor j, and $\overline{x}_j$ and s_j are its complete-data mean and sample standard deviation, respectively. PSI was not externally standardized.

The final prediction equation was:

$$\begin{aligned}\text{Predicted PSI} = 0.000 + 0.321[(\text{GLI} - 0.080)/0.055] + 0.338[(\text{ExG} - 42.165)/32.192] + 0.311[(\text{ExGR} + 9.392)/45.109] - \\ 0.341[(\text{CIVE} - 4.520)/12.704] + 0.324[(\text{g} - 0.371)/0.025]\end{aligned} \quad \text{(A2)}$$

The fitted intercept was -1.80×10^{-16}, which is effectively zero within numerical precision. Positive predicted PSI values indicate positions above the dataset mean along the OJIP-derived latent photochemical axis, whereas negative values indicate positions below the dataset mean. Because PSI is centered, dimensionless, and dataset-dependent, the predicted values should not be interpreted as absolute thresholds of plant health or drought injury.

Table A2. Standardized regression coefficients of the complete-data RGB-based photochemical proxy.

Predictor Variable	Standardized Coefficient
Intercept	-1.80×10^{-16}
GLI	0.321
ExG	0.338
ExGR	0.311
CIVE	−0.341
g	0.324

Table A3. Predictor means and sample standard deviations used for complete-data standardization.

Predictor Variable	Mean	Standard Deviation
GLI	0.080	0.055
ExG	42.165	32.192
ExGR	−9.392	45.109
CIVE	4.520	12.704
g	0.371	0.025

The apparent in-sample fit of the complete-data model is reported in Table A4 only to document the fitted implementation equation. These values are not cross-validated estimates and should not be interpreted as evidence of transferability to unseen species.

Table A4. Apparent in-sample fit of the complete-data RGB-based photochemical proxy.

Metric	Value
R^2	0.519
RMSE	1.509
MAE	1.117

References

1. Mircea, D.-M.; Boscaiu, M.; Sestras, R.E.; Sestras, A.F.; Vicente, O. Abiotic Stress Tolerance and Invasive Potential of Ornamental Plants in the Mediterranean Area: Implications for Sustainable Landscaping. *Agronomy* **2024**, *15*, 52. [CrossRef]
2. Song, Y.; Kim, C.-W.; Kweon, H.; Yoon, K.K.; Shim, Y.-J.; Lee, U.K.; Lee, K.C. Effects of Drought Stress on the Growth and Physiological Characteristics of Grafted Ziziphus jujuba var. inermis under RCP 6.0 Climate Change Scenarios. *Hortic. Sci. Technol.* **2023**, *41*, 11–26. [CrossRef]
3. Toscano, S.; Ferrante, A.; Romano, D. Response of Mediterranean Ornamental Plants to Drought Stress. *Horticulturae* **2019**, *5*, 6. [CrossRef]
4. Joshi, J.; Stocker, B.D.; Hofhansl, F.; Zhou, S.; Dieckmann, U.; Prentice, I.C. Towards a unified theory of plant photosynthesis and hydraulics. *Nat. Plants* **2022**, *8*, 1304–1316. [CrossRef]
5. Dalal, V.K.; Tripathy, B.C. Water-stress induced downsizing of light-harvesting antenna complex protects developing rice seedlings from photo-oxidative damage. *Sci. Rep.* **2018**, *8*, 5955. [CrossRef]
6. Cramer, G.R.; Van Sluyter, S.C.; Hopper, D.W.; Pascovici, D.; Keighley, T.; Haynes, P.A. Proteomic analysis indicates massive changes in metabolism prior to the inhibition of growth and photosynthesis of grapevine (*Vitis vinifera* L.) in response to water deficit. *BMC Plant Biol.* **2013**, *13*, 49. [CrossRef]
7. Hummel, I.; Pantin, F.; Sulpice, R.; Piques, M.; Rolland, G.; Dauzat, M.; Christophe, A.; Pervent, M.; Bouteillé, M.; Stitt, M.; et al. Arabidopsis Plants Acclimate to Water Deficit at Low Cost through Changes of Carbon Usage: An Integrated Perspective Using Growth, Metabolite, Enzyme, and Gene Expression Analysis. *Plant Physiol.* **2010**, *154*, 357–372. [CrossRef]
8. Chaves, M.M.; Flexas, J.; Pinheiro, C. Photosynthesis under drought and salt stress: Regulation mechanisms from whole plant to cell. *Ann. Bot.* **2008**, *103*, 551–560. [CrossRef]
9. Lee, K.C. Changes in Photosynthetic Performance and Water Relation Parameters in the Seedlings of Korean Dendropanax Subjected to Drought Stress. *Korean J. Med. Crop Sci.* **2018**, *26*, 181–187. [CrossRef]
10. Ribeiro, D.; Guzmán, M.R.; Caperta, A.D.; Marques, I. Balancing Osmotic Protection and Oxidative Stress: Physiological and Biochemical Responses of Pot Marigold (*Calendula officinalis* L.) Plants to Water Stress. *Plants* **2025**, *14*, 3809. [CrossRef]
11. Sun, C.; Li, X.; Hu, Y.; Zhao, P.; Xu, T.; Sun, J.; Gao, X. Proline, Sugars, and Antioxidant Enzymes Respond to Drought Stress in the Leaves of Strawberry Plants. *Hortic. Sci. Technol.* **2015**, *33*, 625–632. [CrossRef]
12. Moustakas, M.; Dobrikova, A.; Ivanov, A.G. Editorial: Photosynthesis under abiotic stress. *Front. Plant Sci.* **2025**, *16*, 1732692. [CrossRef]
13. Qiao, M.; Hong, C.; Jiao, Y.; Hou, S.; Gao, H. Impacts of Drought on Photosynthesis in Major Food Crops and the Related Mechanisms of Plant Responses to Drought. *Plants* **2024**, *13*, 1808. [CrossRef]
14. Wang, Z.; Li, G.; Sun, H.; Ma, L.; Guo, Y.; Zhao, Z.; Gao, H.; Mei, L. Effects of drought stress on photosynthesis and photosynthetic electron transport chain in young apple tree leaves. *Biol. Open* **2018**, *7*, bio035279. [CrossRef]
15. Sperdouli, I.; Ouzounidou, G.; Moustakas, M. Hormesis Responses of Photosystem II in Arabidopsis thaliana under Water Deficit Stress. *Int. J. Mol. Sci.* **2023**, *24*, 9573. [CrossRef]
16. Wada, S.; Takagi, D.; Miyake, C.; Makino, A.; Suzuki, Y. Responses of the Photosynthetic Electron Transport Reactions Stimulate the Oxidation of the Reaction Center Chlorophyll of Photosystem I, P700, under Drought and High Temperatures in Rice. *Int. J. Mol. Sci.* **2019**, *20*, 2068. [CrossRef]
17. Jia, Y.; Xiao, W.; Ye, Y.; Wang, X.; Liu, X.; Wang, G.; Li, G.; Wang, Y. Response of Photosynthetic Performance to Drought Duration and Re-Watering in Maize. *Agronomy* **2020**, *10*, 533. [CrossRef]
18. Kim, S.K.; Lee, H.J.; Lee, H.S.; Mun, B.; Lee, S.G. Effect of Soil Water Content on Growth, Photosynthetic Rate, and Stomatal Conductance of Kimchi Cabbage at the Early Growth Stage after Transplanting. *Prot. Hortic. Plant Fact.* **2017**, *26*, 151–157. [CrossRef]
19. Guidi, L.; Lo Piccolo, E.; Landi, M. Chlorophyll Fluorescence, Photoinhibition and Abiotic Stress: Does it Make Any Difference the Fact to Be a C3 or C4 Species? *Front. Plant Sci.* **2019**, *10*, 174. [CrossRef]
20. Moustaka, J.; Moustakas, M. Early-Stage Detection of Biotic and Abiotic Stress on Plants by Chlorophyll Fluorescence Imaging Analysis. *Biosensors* **2023**, *13*, 796. [CrossRef]
21. Akinyemi, O.O.; Čepl, J.; Keski-Saari, S.; Tomášková, I.; Stejskal, J.; Kontunen-Soppela, S.; Keinänen, M. Derivative-based time-adjusted analysis of diurnal and within-tree variation in the OJIP fluorescence transient of silver birch. *Photosynth. Res.* **2023**, *157*, 133–146. [CrossRef]
22. Vredenberg, W. A simple routine for quantitative analysis of light and dark kinetics of photochemical and non-photochemical quenching of chlorophyll fluorescence in intact leaves. *Photosynth. Res.* **2015**, *124*, 87–106. [CrossRef]
23. Kalaji, H.M.; Jajoo, A.; Oukarroum, A.; Brestic, M.; Zivcak, M.; Samborska, I.A.; Cetner, M.D.; Łukasik, I.; Goltsev, V.; Ladle, R.J. Chlorophyll a fluorescence as a tool to monitor physiological status of plants under abiotic stress conditions. *Acta Physiol. Plant.* **2016**, *38*, 102. [CrossRef]

24. Ham, H.D.; Kim, T.S.; Lee, M.H.; Park, K.B.; An, J.-H.; Kang, D.H.; Kim, T.W. The Assessment of Photochemical Index of Nursery Seedlings of Cucumber and Tomato under Drought Stress. *Environ. Biol. Res.* **2018**, *36*, 479–487. [CrossRef]
25. Yoo, S.-Y.; Eom, K.-C.; Park, S.-H.; Kim, T.-W. Possibility of Drought stress Indexing by Chlorophyll Fluorescence Imaging Technique in Red Pepper (*Capsicum annuum* L.). *Korean J. Soil Sci. Fertil.* **2012**, *45*, 676–682. [CrossRef]
26. Oukarroum, A.; Madidi, S.E.; Schansker, G.; Strasser, R.J. Probing the responses of barley cultivars (*Hordeum vulgare* L.) by chlorophyll a fluorescence OLKJIP under drought stress and re-watering. *Environ. Exp. Bot.* **2007**, *60*, 438–446. [CrossRef]
27. Rapacz, M.; Wójcik-Jagła, M.; Fiust, A.; Kalaji, H.M.; Kościelniak, J. Genome-Wide Associations of Chlorophyll Fluorescence OJIP Transient Parameters Connected with Soil Drought Response in Barley. *Front. Plant Sci.* **2019**, *10*, 78. [CrossRef]
28. Botyanszka, L.; Zivcak, M.; Chovancek, E.; Sytar, O.; Barek, V.; Hauptvogel, P.; Halabuk, A.; Brestic, M. Chlorophyll Fluorescence Kinetics May Be Useful to Identify Early Drought and Irrigation Effects on Photosynthetic Apparatus in Field-Grown Wheat. *Agronomy* **2020**, *10*, 1275. [CrossRef]
29. Sánchez-Reinoso, A.D.; Ligarreto-Moreno, G.A.; Restrepo-Díaz, H. Chlorophyll α Fluorescence Parameters as an Indicator to Identify Drought Susceptibility in Common Bush Bean. *Agronomy* **2019**, *9*, 526. [CrossRef]
30. Kim, K.S.; Seo, Y.J.; Kim, D.C.; Nam, H.H.; Lee, B.Y.; Kim, J.h. Effect of Soil Water and Shading Treatment on Chlorophyll Fluorescence Parameters and Photosynthetic Capacity in Cnidium officinale Makino. *Korean J. Med. Crop Sci.* **2020**, *28*, 412–420. [CrossRef]
31. Shin, Y.K.; Jo, J.S.; Cho, M.-C.; Yang, E.-Y.; Ahn, Y.K.; Hwang, I.d.; Lee, J.G. Application of Chlorophyll Fluorescence Parameters to Diagnose Salinity Tolerance in the Seedling of Tomato Genetic Resources. *J. Bio-Environ. Control* **2021**, *30*, 165–173. [CrossRef]
32. Ahlman, L.; Bånkestad, D.; Khalil, S.; Bergstrand, K.-J.; Wik, T. Stress Detection Using Proximal Sensing of Chlorophyll Fluorescence on the Canopy Level. *AgriEngineering* **2021**, *3*, 648–668. [CrossRef]
33. Legendre, R.; Basinger, N.T.; van Iersel, M.W. Low-Cost Chlorophyll Fluorescence Imaging for Stress Detection. *Sensors* **2021**, *21*, 2055. [CrossRef]
34. Shoaib, M.; Khan, S.U.; AbdelHameed, H.; Qahmash, A. Plant stress detection using multimodal imaging and machine learning: From leaf spectra to smartphone applications. *Front. Plant Sci.* **2026**, *16*, 1670593. [CrossRef]
35. Yang, C.; Baireddy, S.; Méline, V.; Cai, E.; Caldwell, D.; Iyer-Pascuzzi, A.S.; Delp, E.J. Image-based plant wilting estimation. *Plant Methods* **2023**, *19*, 52. [CrossRef]
36. Zolin, Y.; Popova, A.; Yudina, L.; Grebneva, K.; Abasheva, K.; Sukhov, V.; Sukhova, E. RGB Indices Can Be Used to Estimate NDVI, PRI, and Fv/Fm in Wheat and Pea Plants Under Soil Drought and Salinization. *Plants* **2025**, *14*, 1284. [CrossRef]
37. Zubler, A.V.; Yoon, J.-Y. Proximal Methods for Plant Stress Detection Using Optical Sensors and Machine Learning. *Biosensors* **2020**, *10*, 193. [CrossRef]
38. Kior, A.; Yudina, L.; Zolin, Y.; Sukhov, V.; Sukhova, E. RGB Imaging as a Tool for Remote Sensing of Characteristics of Terrestrial Plants: A Review. *Plants* **2024**, *13*, 1262. [CrossRef] [PubMed]
39. Al-Tamimi, N.; Langan, P.; Bernád, V.; Walsh, J.; Mangina, E.; Negrão, S. Capturing crop adaptation to abiotic stress using image-based technologies. *Open Biol.* **2022**, *12*, 210353. [CrossRef]
40. Sánchez-Sastre, L.F.; Alte da Veiga, N.M.S.; Ruiz-Potosme, N.M.; Carrión-Prieto, P.; Marcos-Robles, J.L.; Navas-Gracia, L.M.; Martín-Ramos, P. Assessment of RGB Vegetation Indices to Estimate Chlorophyll Content in Sugar Beet Leaves in the Final Cultivation Stage. *AgriEngineering* **2020**, *2*, 128–149. [CrossRef]
41. Khan, Z.; Rahimi-Eichi, V.; Haefele, S.; Garnett, T.; Miklavcic, S.J. Estimation of vegetation indices for high-throughput phenotyping of wheat using aerial imaging. *Plant Methods* **2018**, *14*, 20. [CrossRef]
42. Ruwanpathirana, P.P.; Sakai, K.; Jayasinghe, G.Y.; Nakandakari, T.; Yuge, K.; Wijekoon, W.M.C.J.; Priyankara, A.C.P.; Samaraweera, M.D.S.; Madushanka, P.L.A. Evaluation of Sugarcane Crop Growth Monitoring Using Vegetation Indices Derived from RGB-Based UAV Images and Machine Learning Models. *Agronomy* **2024**, *14*, 2059. [CrossRef]
43. Vit, A.; Shani, G. Comparing RGB-D Sensors for Close Range Outdoor Agricultural Phenotyping. *Sensors* **2018**, *18*, 4413. [CrossRef]
44. Liu, S.; Harris, A.E.; Li, J.; Goggin, F.L.; Mendoza-Cozatl, D.G.; Bucksch, A. SMART: Speedy Measurement of Arabidopsis Rosette Traits. *Plant Phenome J.* **2026**, *9*, e70061. [CrossRef]
45. Das Choudhury, S.; Samal, A.; Awada, T. Leveraging Image Analysis for High-Throughput Plant Phenotyping. *Front. Plant Sci.* **2019**, *10*, 508. [CrossRef] [PubMed]
46. Bak, H.-J.; Kim, E.-J.; Lee, J.-H.; Chang, S.; Kwon, D.; Im, W.-J.; Hwang, W.-H.; Chang, J.-K.; Chung, N.-J.; Sang, W.-G. Deep learning-based semantic segmentation for rice yield estimation by analyzing the dynamic change of panicle coverage. *Front. Plant Sci.* **2025**, *16*, 1611653. [CrossRef]
47. Lee, U.; Chang, S.; Putra, G.A.; Kim, H.; Kim, D.H. An automated, high-throughput plant phenotyping system using machine learning-based plant segmentation and image analysis. *PLoS ONE* **2018**, *13*, e0196615. [CrossRef]
48. Gill, T.; Gill, S.K.; Saini, D.K.; Chopra, Y.; de Koff, J.P.; Sandhu, K.S. A Comprehensive Review of High Throughput Phenotyping and Machine Learning for Plant Stress Phenotyping. *Phenomics* **2022**, *2*, 156–183. [CrossRef]

49. Tharuka, M.V.T.; Kularathna, K.M.; Ray, R.L. Application of RGB-Imaging techniques for high-throughput plant phenotyping- A Review. *Turk. J. Agric.-Food Sci. Technol.* **2025**, *13*, 3678–3686. [CrossRef]
50. Lee, S.-J.; Han, S.-W.; Kim, T.-W.; Yoo, S.-Y. RGB image-based drought stress classification of garden plants using SVM model. *Sci. Rep.* **2026**, *16*, 21087. [CrossRef]
51. Lee, S.J.; Kim, T.W.; Eom, T.S.; Yoon, T.J.; Hwang, Y.B.; Seo, J.Y.; Yoo, S.Y. Identification of Chlorophyll Fluorescence Parameters for Evaluating Drought Stress in Garden Plants. *J. People Plants Environ.* **2025**, *28*, 601–613. [CrossRef]
52. Zarcotejada, P.; Berjon, A.; Lopezlozano, R.; Miller, J.; Martin, P.; Cachorro, V.; Gonzalez, M.; Defrutos, A. Assessing vineyard condition with hyperspectral indices: Leaf and canopy reflectance simulation in a row-structured discontinuous canopy. *Remote Sens. Environ.* **2005**, *99*, 271–287. [CrossRef]
53. Louhaichi, M.; Borman, M.M.; Johnson, D.E. Spatially Located Platform and Aerial Photography for Documentation of Grazing Impacts on Wheat. *Geocarto Int.* **2001**, *16*, 65–70. [CrossRef]
54. Tucker, C.J. Red and photographic infrared linear combinations for monitoring vegetation. *Remote Sens. Environ.* **1979**, *8*, 127–150. [CrossRef]
55. Woebbecke, D.M.; Meyer, G.E.; Bargen, K.V.; Mortensen, D.A. Color Indices for Weed Identification Under Various Soil, Residue, and Lighting Conditions. *Trans. ASAE* **1995**, *38*, 259–269. [CrossRef]
56. Meyer, G.E.; Neto, J.C. Verification of color vegetation indices for automated crop imaging applications. *Comput. Electron. Agric.* **2008**, *63*, 282–293. [CrossRef]
57. Kataoka, T.; Kaneko, T.; Okamoto, H.; Hata, S. Crop growth estimation system using machine vision. In *Proceedings of the 2003 IEEE/ASME International Conference on Advanced Intelligent Mechatronics (AIM 2003), Kobe, Japan, 20–24 July 2003*; IEEE: Piscataway, NJ, USA, 2003; pp. b1079–b1083.
58. Gitelson, A.A.; Kaufman, Y.J.; Stark, R.; Rundquist, D. Novel algorithms for remote estimation of vegetation fraction. *Remote Sens. Environ.* **2002**, *80*, 76–87. [CrossRef]
59. Abdi, H. Partial least squares regression and projection on latent structure regression (PLS Regression). *WIREs Comput. Stat.* **2010**, *2*, 97–106. [CrossRef]
60. Geladi, P.; Kowalski, B.R. Partial least-squares regression: A tutorial. *Anal. Chim. Acta* **1986**, *185*, 1–17. [CrossRef]
61. R Core Team. *R: A Language and Environment for Statistical Computing*, version 4.1.2; R Foundation for Statistical Computing: Vienna, Austria, 2021.
62. Shanker, A.K.; Amirineni, S.; Bhanu, D.; Yadav, S.K.; Jyothilakshmi, N.; Vanaja, M.; Singh, J.; Sarkar, B.; Maheswari, M.; Singh, V.K. High-resolution dissection of photosystem II electron transport reveals differential response to water deficit and heat stress in isolation and combination in pearl millet [*Pennisetum glaucum* (L.) R. Br.]. *Front. Plant Sci.* **2022**, *13*, 892676. [CrossRef]
63. Weng, H.; Liu, Y.; Captoline, I.; Li, X.; Ye, D.; Wu, R. Citrus Huanglongbing detection based on polyphasic chlorophyll a fluorescence coupled with machine learning and model transfer in two citrus cultivars. *Comput. Electron. Agric.* **2021**, *187*, 106289. [CrossRef]
64. Zhou, R.; Kan, X.; Chen, J.; Hua, H.; Li, Y.; Ren, J.; Feng, K.; Liu, H.; Deng, D.; Yin, Z. Drought-induced changes in photosynthetic electron transport in maize probed by prompt fluorescence, delayed fluorescence, P700 and cyclic electron flow signals. *Environ. Exp. Bot.* **2019**, *158*, 51–62. [CrossRef]
65. Alexandrina Stirbet, G. On the relation between the Kautsky effect (chlorophyll a fluorescence induction) and Photosystem II: Basics and applications of the OJIP fluorescence transient. *J. Photochem. Photobiol. B Biol.* **2011**, *104*, 236–257. [CrossRef]
66. Strasser, R.J.; Tsimilli-Michael, M.; Srivastava, A. Analysis of the Chlorophyll a Fluorescence Transient. In *Chlorophyll a Fluorescence*; Advances in Photosynthesis and Respiration; Springer: Dordrecht, The Netherlands, 2004; pp. 321–362. [CrossRef]
67. Strasser, R.J.; Srivastava, A.; Tsimilli-Michael, M. The fluorescence transient as a tool to characterize and screen photosynthetic samples. *Probing Photosynth. Mech. Regul. Adapt.* **2000**, *25*, 445–483.
68. Tsimilli-Michael, M. Special issue in honour of Prof. Reto J. Strasser—Revisiting JIP-test: An educative review on concepts, assumptions, approximations, definitions and terminology. *Photosynthetica* **2020**, *58*, 275–292. [CrossRef]
69. Jolliffe, I.T.; Cadima, J. Principal component analysis: A review and recent developments. *Philos. Trans. R. Soc. A Math. Phys. Eng. Sci.* **2016**, *374*, 20150202. [CrossRef] [PubMed]
70. Abdi, H.; Williams, L.J. Principal component analysis. *WIREs Comput. Stat.* **2010**, *2*, 433–459. [CrossRef]
71. Yang, Y.; Nan, R.; Mi, T.; Song, Y.; Shi, F.; Liu, X.; Wang, Y.; Sun, F.; Xi, Y.; Zhang, C. Rapid and Nondestructive Evaluation of Wheat Chlorophyll under Drought Stress Using Hyperspectral Imaging. *Int. J. Mol. Sci.* **2023**, *24*, 5825. [CrossRef]
72. Hu, F.; Zhang, Y.; Guo, J. Effects of drought stress on photosynthetic physiological characteristics, leaf microstructure, and related gene expression of yellow horn. *Plant Signal. Behav.* **2023**, *18*, 2215025. [CrossRef]
73. Batra, N.G.; Sharma, V.; Kumari, N. Drought-induced changes in chlorophyll fluorescence, photosynthetic pigments, and thylakoid membrane proteins of *Vigna radiata*. *J. Plant Interact.* **2014**, *9*, 712–721. [CrossRef]

74. Ashikhmin, A.; Bolshakov, M.; Pashkovskiy, P.; Vereshchagin, M.; Khudyakova, A.; Shirshikova, G.; Kozhevnikova, A.; Kosobryukhov, A.; Kreslavski, V.; Kuznetsov, V.; et al. The Adaptive Role of Carotenoids and Anthocyanins in Solanum lycopersicum Pigment Mutants under High Irradiance. *Cells* **2023**, *12*, 2569. [CrossRef]
75. Gitelson, A.A.; Gritz, Y.; Merzlyak, M.N. Relationships between leaf chlorophyll content and spectral reflectance and algorithms for non-destructive chlorophyll assessment in higher plant leaves. *J. Plant Physiol.* **2003**, *160*, 271–282. [CrossRef]
76. Niu, Y.; Xu, X.; Huang, W.; Li, J.; Li, S.; Zhao, N.; Li, B.; Xu, C.; Lu, S. RGB Imaging and Irrigation Management Reveal Water Stress Thresholds in Three Urban Shrubs in Northern China. *Plants* **2025**, *14*, 2253. [CrossRef]
77. Yuan, Y.; Wang, X.; Shi, M.; Wang, P. Performance comparison of RGB and multispectral vegetation indices based on machine learning for estimating Hopea hainanensis SPAD values under different shade conditions. *Front. Plant Sci.* **2022**, *13*, 928953. [CrossRef]
78. Guo, Y.; Wang, H.; Wu, Z.; Wang, S.; Sun, H.; Senthilnath, J.; Wang, J.; Robin Bryant, C.; Fu, Y. Modified Red Blue Vegetation Index for Chlorophyll Estimation and Yield Prediction of Maize from Visible Images Captured by UAV. *Sensors* **2020**, *20*, 5055. [CrossRef]
79. Yoon, T.; Kim, T.; Yoo, S. Non-Destructive Drone-Based Multispectral and RGB Image Analyses for Regression Modeling to Assess Waterlogging Stress in Pseudolysimachion linariifolium. *Horticulturae* **2025**, *11*, 1139. [CrossRef]
80. Sang, W.-G.; Kim, J.-H.; Baek, J.-K.; Kwon, D.; Ban, H.-Y.; Cho, J.-I.; Seo, M.-C. Detection of Drought Stress in Soybean Plants using RGB-based Vegetation Indices. *Korean J. Agric. For. Meteorol.* **2021**, *23*, 340–348. [CrossRef]
81. Starý, K.; Jelínek, Z.; Kumhálová, J.; Chyba, J.; Balážová, K. Comparing RGB-based vegetation indices from UAV imageries to estimate hops canopy area. *Agron. Res.* **2020**, *18*, 2592–2601. [CrossRef]
82. Bendig, J.; Bolten, A.; Bennertz, S.; Broscheit, J.; Eichfuss, S.; Bareth, G. Estimating biomass of barley using crop surface models (CSMs) derived from UAV-based RGB imaging. *Remote Sens.* **2014**, *6*, 10395–10412. [CrossRef]
83. Murchie, E.H.; Lawson, T. Chlorophyll fluorescence analysis: A guide to good practice and understanding some new applications. *J. Exp. Bot.* **2013**, *64*, 3983–3998. [CrossRef]
84. Baker, N.R. Chlorophyll Fluorescence: A Probe of Photosynthesis In Vivo. *Annu. Rev. Plant Biol.* **2008**, *59*, 89–113. [CrossRef] [PubMed]
85. Abebe, A.M.; Kim, Y.; Kim, J.; Kim, S.L.; Baek, J. Image-Based High-Throughput Phenotyping in Horticultural Crops. *Plants* **2023**, *12*, 2061. [CrossRef]
86. Fahlgren, N.; Gehan, M.A.; Baxter, I. Lights, camera, action: High-throughput plant phenotyping is ready for a close-up. *Curr. Opin. Plant Biol.* **2015**, *24*, 93–99. [CrossRef]